



National Library of Canada

Bibliothèque nationale du Canada

CANADIAN THESES ON MICROFICHE

THÈSES CANADIENNES SUR MICROFICHE

NAME OF AUTHOR/NOM DE L'AUTEUR Klaus Hartmann Wanke

TITLE OF THESIS/TITRE DE LA THÈSE High Resolution Phase Contrast Electron Microscopy

UNIVERSITY/UNIVERSITÉ University of Alberta

DEGREE FOR WHICH THESIS WAS PRESENTED/ GRADE POUR LEQUEL CETTE THÈSE FUT PRÉSENTÉE M.Sc.

YEAR THIS DEGREE CONFERRED/ANNÉE D'OBTENTION DE CE GRADE 1975

NAME OF SUPERVISOR/NOM DU DIRECTEUR DE THÈSE Dr. S. S. Klein

Permission is hereby granted to the NATIONAL LIBRARY OF CANADA to microfilm this thesis and to lend or sell copies of the film.

L'autorisation est, par la présente, accordée à la BIBLIOTHÈQUE NATIONALE DU CANADA de microfilmer cette thèse et de prêter ou de vendre des exemplaires du film.

The author reserves other publication rights, and neither the thesis nor extensive extracts from it may be printed or otherwise reproduced without the author's written permission.

L'auteur se réserve les autres droits de publication; ni la thèse ni de longs extraits de celle-ci ne doivent être imprimés ou autrement reproduits sans l'autorisation écrite de l'auteur.

DATED/DATE July 14, 1975 SIGNED/SIGNÉ K. Wanke

PERMANENT ADDRESS/RÉSIDENCE FIXE Site 11, Box 14  
RR2 Sherwood Park  
Alberta, Canada

THE UNIVERSITY OF ALBERTA

HIGH RESOLUTION PHASE CONTRAST ELECTRON MICROSCOPY

by



KLAUS HARTMUTH WANKE

A THESIS

SUBMITTED TO THE FACULTY OF GRADUATE STUDIES AND RESEARCH  
IN PARTIAL FULFILLMENT OF THE REQUIREMENTS FOR THE DEGREE  
OF MASTER OF SCIENCE

DEPARTMENT OF PHYSICS


EDMONTON, ALBERTA


FALL, 1975


THE UNIVERSITY OF ALBERTA

FACULTY OF GRADUATE STUDIES AND RESEARCH

The undersigned certify that they have read,  
and recommend to the Faculty of Graduate Studies and  
Research, for acceptance, a thesis entitled HIGH  
RESOLUTION PHASE CONTRAST ELECTRON MICROSCOPY submitted  
by Klaus Hartmuth Wanke in partial fulfillment of the  
requirements for the degree of Master of Science.

  
.....  
Supervisor

  
.....

  
.....

.....

Date: July 2, 1975

## ABSTRACT

High resolution transmission electron microscopy using phase contrast techniques can be used to obtain images corresponding to the projected electrostatic potential of large unit cell materials. The possibility of obtaining such images of small unit cell specimens was investigated for the case of thin crystals. A high resolution electron microscope was calibrated in the course of the investigation. Suitable conditions could not be obtained for crystal lattice spacings of less than .5 nm.

## ACKNOWLEDGEMENTS

I wish to express my gratitude to Dr. P.S. Turner and to Dr. S.S. Sheinin for supervising the project and for their assistance and patience.

I would like to acknowledge the technical expertise of Mr. J.C. Brunel and his care of the microscope.

Thanks also to my friends Don McGillvray, John Andrew, and Kamal Botros for their suggestions and assistance.

For the typing of this manuscript I wish to thank Mrs. Mary Yiu.

I also wish to express my appreciation to Martin Semrok for the use of his enlarger and for his help with the production of the final prints.

Finally, I wish to thank Uta Semrok for her encouragement and patience.

## TABLE OF CONTENTS

	<u>Page</u>
CHAPTER 1 INTRODUCTION	1
CHAPTER 2 THEORY	7
2.1 Introduction	7
2.2 Aberration Theory	9
2.3 Phase Differences	15
2.4 Lattice Imaging, Phase Contrast and Optimum Defocus	19
2.5 Transfer Theory	25
2.6 Chromatic Aberration	27
CHAPTER 3 EXPERIMENTAL PROCEDURE	32
3.1 Specimens and Specimen Preparation	32
3.2 Calibration	34
3.2.1 Magnification	35
3.2.2 Camera Length	38
3.2.3 Defocus Dependence on Current Change	39
3.2.4 Defocus Per Click	41
3.2.5 Chromatic Aberration	43
3.2.6 Spherical Aberration	44
CHAPTER 4 DISCUSSION	49

	<u>Page</u>
REFERENCES	78
APPENDIX I THE LIGHT OPTICAL DIFFRACTOMETER	81
APPENDIX II ANALYSIS OF OBJECTIVE LENS CURRENT CONTROL CIRCUIT	83

## LIST OF FIGURES

<u>Figure</u>		<u>Page</u>
1	Schematic diagram of an optical system	53
2	Diagram of spherical aberration	54
3	Detailed diagram of spherical aberration	55
4	Detailed diagram of defocussing	55
5	The effects of various phase shifts	56
6	Phase shift as a function of scattering angle for $C_s = 1.7$ mm and various defocus values	56
7	Transmitted spatial periodicities as a function of defocus for $C_s = 1.7$ mm.	57
8	The transfer function at optimum defocus	57-58
9	The transfer function at a non-optimum defocus	58-59
10	Optimum defocus as a function of spherical aberration	59
11	Diagram of the z-stage	60
12	The structure of bismuth oxychloride	60
13	Lattice images of BiOCl	61
14	Position of optic axis for obtaining crossed lattice fringes	62
15	Crossed lattice images of BiOCl	62
16	Magnification as a function of objective lens current	63
17	Magnification as a function of specimen height	63
18	Camera length as a function of objective lens current	64



<u>Figure</u>		<u>Page</u>
19	Plot of specimen height against objective lens current	64
20	Defocus dependence on current change	65
21	Doubly exposed micrographs of MgO crystals in untilted dark field mode	66
22	Change in lens current per click of medium knob	67
23	Change in lens current per click of fine medium knob	67
24	Change in lens current per click of second finest knob	68
25	Change of lens current per click of finest knob	69
26	Defocus per click of medium knob	70
27	Defocus per click of fine medium knob	70
28	Defocus per click of second finest knob	71
29	Defocus per click of finest knob	71
30	Upper limit of the chromatic aberration plotted against lens current	72
31	Photograph of amorphous carbon and corresponding diffractogram	72
32	Plot of spherical aberration as a function of lens current	73
33	Examples of spherical aberration measurements	74
34	Three-fold crossed lattice fringes of biotite	75
35	Edge on views of muscovite and biotite	76
36	Circuit diagram of objective lens focussing circuit	77

## CHAPTER 1

### INTRODUCTION

This thesis reports work done in the field of high resolution transmission electron microscopy, with the aim of investigating conditions under which useful structural information may be obtained from crystalline materials. An important part of the project involved the calibration of a high resolution electron microscope. The possibility of obtaining images which relate in a simple way to crystal structure was investigated for the case of thin crystals. Suitable conditions could not be obtained for crystal lattice spacings of about .25 nm.

Even the early electron microscopists were interested in the problem of high resolution. But not until recently have single atoms in certain molecules been imaged successfully. For crystals, the techniques of lattice imaging and phase contrast are well known, but again, not until recently have they been used to obtain structural information at the unit cell level.

It was shown by Rebsch as early as 1938 that the resolution limit of an electron microscope is not determined by the wavelength  $\lambda$  of the illuminating

2

radiation as given by Abbé's theory:

$$d = 0.6 \lambda / \sin \alpha \quad (1)$$

( $\alpha$  is the aperture angle of the objective lens)

Rather the resolution limit is a compromise between diffraction and the spherical aberration of the magnetic lenses. Scherzer (1949) found the resolution to be limited by spherical aberration according to the formula

$$d = k \lambda^{0.75} C_s^{0.25} \quad (2)$$

where  $C_s$  = spherical aberration coefficient and the constant  $k$  has values between 0.43 and 0.98 for various imaging conditions. He also calculated an "optimum defocus condition" for best contrast, taking into account phase cancellations between beams scattered at various angles. Eisenhandler and Siegel (1966), Hall and Hines (1970), and Reimer (1969) have done similar but more detailed calculations for isolated atoms, for linear atomic chains, and for clusters of atoms.

As the electron microscope has been gradually improved by many small technical changes over the years, the resolution limit has been reduced sufficiently to image heavy atoms on a low noise substrate. Thus Prestridge and Yates (1971) have claimed to have imaged

rhodium atoms on silica. Various heavy atoms attached to complex molecules on thin carbon substrates have been seen by Henkelman and Ottensmeyer (1971) in the dark field mode. Hashimoto and colleagues (1971, 1973) reported the visualization of thorium atoms on graphite, also in dark field. This was confirmed by Phillips, Chalk, and Hugo (1972). Formanek et al (1971) observed a triangular arrangement of mercury atoms in the compound triacetoxymercury aurine using bright field imaging. Thon and Willasch (1972) succeeded in imaging the same arrangement using hollow cone illumination. Parsons and co-workers (1973) have obtained contrast reversals of images of uranium atoms in stained molecules of mellitic acid for different defocus conditions. When signal processing is applied to electron micrographs, atoms as light as sulfur can be revealed, as was shown by Ottensmeyer, Schmidt, and Olbrecht (1973).

The problem of imaging the single atoms in a crystal is somewhat different. Crystals, in general, have thickness, i.e., they consist of more than one layer. Therefore at best only a projection of the crystal structure can be imaged. Materials with a periodic structure give rise to diffraction patterns of discrete spots. The electron microscopist thus can include or omit parts of the wave emerging from the

exit face of the crystal quite precisely. Clearly, the more spots or beams that are allowed to contribute to the image, the more information is recorded. Just two beams can give rise to a pattern of apparent lattice planes of the specimen material crossing the image. Three collinear beams can generate a similar pattern as Menter (1956) showed when the technique was first introduced. Such sinusoidal intensity variations across the image are indeed caused by the lattice planes and may even show contrast effects due to edge dislocations, boundary strain, and other defects in the crystal. However, the fringes are generally displaced from the lattice planes which generated them. Indeed, they shift as the focus is changed. Fringes can also be found beyond the edge of a crystal (Hashimoto and Watanabe, 1960). Cowley (1959) and Hashimoto, Mannami and Naiki (1961) showed that the fringe spacing varies slightly from the actual crystal lattice spacing when the diffracted beam is not exactly in the Bragg condition. The number and position of terminating fringe images has been shown to depend on the diffraction geometry (Cockayne, Parsons, Hoelke, 1971). Thus it is not correct to assume one-to-one correspondence between lattice fringes and the actual lattice planes of the specimen.

When examining a tetragonal material, the illumination can be tilted so that the optic axis is equidistant from four beams: the (000), (110), ( $1\bar{1}0$ ), and (200) beams, for example. (See Figure (14)). If only these four beams are allowed to recombine in the image plane, it is possible to generate crossed lattice images. The dots thus obtained may look like images of atoms, but to identify them as such is not warranted.

If many beams contribute to the image, even more complex patterns can be generated, provided phase contrast effects are taken into account (Cowley and Iijima, 1972). Allpress and Sanders (1973) have studied defects in heavily faulted complex oxide structures with large unit cells in this way. They concluded that under favourable circumstances there is a direct correspondence between image contrast and crystal structure at the near atomic level. This correspondence can be described by the projected potential approximation to the image formation theory of Cowley and Moodie (1957, 1958, 1959a,b). The favourable circumstances necessary are that a large number of beams be allowed to contribute to the image; that the objective aperture be symmetrically placed about the central beam; and that the structural features of interest be properly projected.

The possibility of extending the projected potential approximation to materials with small unit cells is

examined in this M.Sc. project. In addition, the project was designed to provide experience with the electron microscope and electron microscopy techniques; to study the problem of high resolution electron microscopy; and to attempt the imaging of individual atoms in a crystal. Thus the next chapter discusses the relevant theory of electron microscope imaging: aberration theory, phase contrast theory and optimum defocus conditions, transfer theory, and the projected potential approximation. Chapter three deals with the experimental procedure: with specimen preparation, and with the calibration of the electron microscope. A discussion of the results obtained is found in chapter four.

## CHAPTER 2

### THEORY

#### 2.1 Introduction

The optical characteristics of an electron microscope can be described using the terminology of light optics. This analogy is possible because quantum mechanics associates a wavelength  $\lambda$  with a moving electron:

$$\lambda = h/p \quad (3)$$

( $p$  = momentum,  $h$  = Planck's constant)

A moving electron can also be focussed using magnetic fields. The effect of such fields on electrons can be described by a refractive index  $n$ . Thus the lens action of an electron microscope can be explained in terms of geometrical optics and wave optics.

However, light optics and electron optics are not completely analogous. Magnetic lenses provide only converging lens action. This makes it difficult to correct for aberrations, especially for spherical and chromatic aberrations. In fact neither has been usefully corrected at high magnifications to date. Another difference is the interaction of electrons with matter. Atoms can easily deflect electrons. Thus the microscope



column is evacuated and the specimen is maintained in vacuum. Although the specimens used are very thin, the electrons must still be accelerated to high energies in order to make it possible for most of them to penetrate the specimens. The majority of the electrons that are then scattered by the specimen are scattered at small angles. Those scattered at large angles are strongly affected by the aberrations of the magnetic lenses. Thus the useful focussing action is only of small angles (less than about  $1^\circ$ ). In contrast, light microscopes use angles of up to  $80^\circ$ .

Since only small angles are encountered in electron focussing, the paraxial approximation is useful and valid in all but high resolution work. Snell's law

$$n_1 \sin \theta_1 = n_2 \theta_2$$

can be approximated by

$$n_1 \theta_1 = n_2 \theta_2 \quad (4)$$

when  $\sin \theta = \theta$  to sufficient accuracy. The optical system then gives "ideal lens action". Here  $n_1$  and  $n_2$  are indices of refraction;  $\theta_1$  and  $\theta_2$  are angles of incidence and refraction, as usual. At high resolution, however, such accuracy is not sufficient so the next term in the expansion of  $\sin \theta$  must be considered:

$$\sin \theta = \theta - \theta^3/3! \quad (5)$$

The extra term gives rise to the "third order aberrations" or departures from ideal lens action. These include coma, astigmatism, curvature of field, distortion, and spherical aberration. All except spherical aberration are negligible in electron microscopy at high magnifications. A derivation of the third order aberrations is given in El-Kareh and El-Kareh (1970). An outline of that derivation is given in the next section. Spherical aberration causes phase changes in the outgoing wave. The contrast effects arising from this and from defocus are discussed in the later sections of the chapter. Chromatic aberration is also discussed.

## 2.2 Aberration Theory

Consider a rotationally symmetric optical system, such as in Figure (1). Introduce sets of mutually parallel rectangular Cartesian coordinates in the object, aperture, and image planes. Let the origins be on the optic axis, which is also the z-direction, so that the object plane is at  $z_0$ , the aperture plane at  $z_a$ , and the image plane at  $z_i$ . The region between the aperture plane and the image plane is assumed to be field free. Let a ray starting from  $P_0(x, y)$  in the

object plane intersect the aperture plane at  $P_a(u,v)$  and the Gaussian image plane at  $P_i(X,Y)$ . The aperture plane is the back focal plane. The Gaussian image plane is the plane at which an infocus image, without aberrations, would form if all rays emanating from the object plane obeyed equation (4).

An ideal lens system will change spherical wave surfaces emanating from  $P_o$  to spheres converging on the Gaussian image point  $P'_i$ . In practice, the converging wave fronts will only approximate a sphere. A ray starting from  $P_o$  will miss  $P'_i$  and arrive instead at  $P_i$ . The distance  $\Delta R = P'_i - P_i$  is called the ray aberration.

From Fermat's principle, the optical path length of a ray going from  $P_o$  to  $P_i$  will be

$$S = \int_{P_o}^{P_i} n \, ds, \quad S \text{ a minimum} \quad (6)$$

where  $n$  is the refractive index of the medium along the path. The path of any electron from point  $P_o(x,y)$  in the object plane through point  $P_a(u,v)$  of the aperture plane to  $P_i(X,Y)$  of the image plane is uniquely determined. Thus  $S$  can be written as a power series in the coordinates  $x,y,u,v$ :

$$S_o = S_o + a_1x + a_2y + a_3u + a_4v + b_1x^2 + b_2xy + \dots \quad (7)$$

or 
$$S = S_o + S_1 + S_2 + S_3 + S_4 + \dots$$

where  $S_n$  denotes the  $n^{\text{th}}$  order terms in the coordinates. Since the system is rotationally symmetric, the optical distance  $S$  remains invariant if the whole system is rotated. As a result all odd  $S_n$  must be zero, i.e.,

$$S = S_0 + S_2 + S_4 + \dots \quad (8)$$

The rotational symmetry requirement also reduces the number of terms in each of  $S_2$  and  $S_4$ . If the object coordinate system is then rotated with respect to the aperture plane by a judicious amount, the equations can be further simplified. For example,

$$S_2 = b_1(x^2 + y^2) + b_4(xu + yv) + b_8(u^2 + v^2).$$

Now  $S = \int n \, ds$  implies  $|\text{grad } S| = n$ . The direction cosines of a ray are given by

$$\cos \alpha = \frac{\partial S / \partial x}{|\text{grad } S|}, \quad \cos \beta = \frac{\partial S / \partial y}{|\text{grad } S|}, \quad \cos \gamma = \frac{\partial S / \partial z}{|\text{grad } S|}$$

(9)

or

$$\cos \alpha = \frac{1}{n} \frac{\partial S}{\partial u}, \quad \cos \beta = \frac{1}{n} \frac{\partial S}{\partial v}, \quad \cos \gamma = \frac{1}{n} \frac{\partial S}{\partial z_a} \quad (10)$$

for a ray with respect to the aperture plane. Since the region beyond the aperture plane is field free the direction cosines are also given by

$$\cos \alpha = (X-u) / [(X-u)^2 + (Y-v)^2 + (z_i - z_a)^2]^{0.5}, \text{ etc.} \quad (11)$$

Therefore

$$X = u + \frac{1}{n} \frac{\partial S}{\partial u} [(X-u)^2 + (Y-v)^2 + (z_i - z_a)^2]^{0.5}$$

or

$$X = u + \frac{z}{n} \frac{\partial S}{\partial u} \left( \frac{(X-u)^2}{z^2} + \frac{(Y-v)^2}{z^2} + 1 \right)^{0.5} \quad (12)$$

where  $z = z_i - z_a$ . The term in brackets can be expanded as

$$1 + \frac{(X-u)^2}{2z^2} + \frac{(Y-v)^2}{2z^2} + \dots$$

In the Gaussian approximation only the first term is taken:

$$X_1 = u + \frac{z}{n} \frac{\partial S_2}{\partial u}$$

Similarly,

$$Y_1 = v + \frac{z}{n} \frac{\partial S_2}{\partial v} \quad (13)$$

Third order theory gives

$$X_3 = u + \frac{z}{n} \left( \frac{\partial S_2}{\partial u} + \frac{\partial S_4}{\partial u} \right) \left( 1 + \frac{(X-u)^2}{2z^2} + \frac{(Y-v)^2}{2z^2} \right) \quad (14)$$

$$Y_3 = v + \frac{z}{n} \left( \frac{\partial S_2}{\partial v} + \frac{\partial S_4}{\partial v} \right) \left( 1 + \frac{(X-u)^2}{2z^2} + \frac{(Y-v)^2}{2z^2} \right)$$

The subscript refers to the order of the approximation. The difference between the first order and third order equations is the expression for the third order aberrations:

$$\Delta X = X_3 - X_1 = \frac{1}{n} \frac{\partial S_2}{\partial u} \left( \frac{(X_1 - u)^2}{2Z} + \frac{(Y_1 - v)^2}{2Z} \right) + \frac{z}{n} \frac{\partial S_4}{\partial u} \quad (15)$$

$$\Delta Y = Y_3 - Y_1 = \frac{1}{n} \frac{\partial S_2}{\partial v} \left( \frac{(X_1 - u)^2}{2Z} + \frac{(Y_1 - v)^2}{2Z} \right) + \frac{z}{n} \frac{\partial S_4}{\partial v}$$

Differentiating  $S_2$  and  $S_4$  gives:

$$\begin{aligned} \Delta X = & Ax(x^2 + y^2) - By(x^2 + y^2) + Cu(x^2 + y^2) + D[u(x^2 - y^2) + 2xyv] \\ & + E[v(x^2 - y^2) - 2uyx] + F[x(3u^2 + v^2) + 2yuv] \\ & + G[-y(3u^2 + v^2) + 2xuv] + Hu(u^2 + v^2) \end{aligned} \quad (16)$$

$$\begin{aligned} \Delta Y = & Ay(x^2 + y^2) + Bx(x^2 + y^2) + Cv(x^2 + y^2) + D[-v(x^2 - y^2) + 2xyu] \\ & + E[u(x^2 - y^2) + 2vxy] + F[y(3v^2 + u^2) + 2xuv] \\ & + G[x(3v^2 + u^2) - 2yuv] + Hv(u^2 + v^2) \end{aligned}$$

The coefficients A to H are introduced after collecting the various terms. For example,  $H = 4Zc_{10}n^{-1} - 1/2Z^2$ . The terms of the expressions can now be identified with the various aberrations that are observed in optical instruments. Thus

A and B are distortion terms

C represents curvature of field

D and E<sub>0</sub> cause geometrical astigmatism

F and G are coma coefficients

H is the term which gives rise to spherical aberration.

It can be seen that spherical aberration is the only third order aberration which does not depend on the position of the object and thus does not vanish even for axial objects. It is the only one that remains at high magnifications:

$$\Delta X = Hu(u^2 + v^2) \quad (17)$$

$$\Delta Y = Hv(u^2 + v^2)$$

The ray aberration  $\Delta R$  therefore is

$$\begin{aligned} \Delta R &= (\Delta X^2 + \Delta Y^2)^{0.5} = H[(u^2 + v^2)^2 u^2 + (u^2 + v^2)^2 v^2]^{0.5} \\ &= H(u^2 + v^2)^{1.5} = H q^3 \end{aligned} \quad (18)$$

where  $q^2 = u^2 + v^2$ . Thus spherical aberration is proportional to the cube of the distance from the optic axis at which an electron passes the back focal plane.

The situation as encountered in the electron microscope is that non-paraxial rays are refracted more strongly than paraxial rays. See Figure (2).

They focus in front of the Gaussian image plane. In the Gaussian image plane, the paraxial rays produce a point image, but the aberrated rays form a circle of confusion of radius  $\Delta R$ . Referred to the object plane, the radius of the confusion circle is

$$\Delta r = \Delta R/M = H q_o^3/M = H f^3 \alpha_o^3/M = C_s \alpha_o^3. \quad (19)$$

Here  $M$  is the magnification,  $f$  is a constant approximately equal to the focal length,  $C_s = H f^3/M$  is the spherical aberration coefficient,  $\alpha_o$  is the largest scattering angle that can pass through the objective aperture. It corresponds to the largest allowed radius in the back focal plane  $q_o = f \tan \alpha_o$ . The approximation  $\tan^3 \alpha = \alpha^3$  was made since all other terms are of higher than third order.

The spherical aberration coefficient of a rotationally symmetric lens is always positive. This was shown by Scherzer (1936). Another derivation is given in El Karez and El Karez (1970), chapter 10. Spherical aberration can be reduced by using octopole lenses or electrostatic mirrors, but neither method has been practically realized.

### 2.3 Phase Differences

Two rays, an ideal paraxial ray and a ray encountering spherical aberration, which leave the



same object point in phase will arrive at the image plane out of phase. Thus the ray AVC of Figure (3) will have its phase delayed with respect to AVD, because of the longer path AVC travels. The optical path length difference  $W$  (called the wave aberration) is given by Born and Wolf (1970) on page 206, equations (10) as:

$$\Delta X = \frac{R'}{n} \frac{\partial W}{\partial u} \quad (20)$$

$$\Delta Y = \frac{R'}{n} \frac{\partial W}{\partial v}$$

where  $n$  is the refractive index of image space.  $R'$  is to a good approximation the distance between the back focal plane and the Gaussian image plane. Therefore

$$\begin{aligned} W &= H n (u^2 + v^2)^2 / 4R' \\ &= H n q^4 / 4R' \\ &= H n f^4 \alpha^4 / 4R' \\ &= n C_S M f \alpha^4 / 4R' \\ &= C_S \alpha^4 / 4 \end{aligned} \quad (21)$$

since  $R'/nf = M$ . Thus a ray suffering from spherical aberration will arrive at the image plane with a phase retarded by  $(2\pi/\lambda) C_S \alpha^4 / 4$  with respect to its Gaussian approximation.

A ray can also be phase shifted by defocussing or overfocussing. Consider the infocus paraxial ray BVE in Figure (4). If defocus  $\Delta f$  is introduced ( $\Delta f$  positive, i.e., lens weakened), then the ray takes the path BVF. It arrives at F where the infocus ray AVF previously arrived. Thus a circle of confusion occurs in the object plane of radius

$$AB = \Delta f \tan \alpha \cong \Delta f \alpha \quad (22)$$

In the image plane the radius of the confusion circle, i.e., the shift of the beam is

$$EF' = \Delta R = M \Delta f \alpha \quad (23)$$

Equations (20) also apply in this case so the wave aberration associated with a defocus  $\Delta f$  is

$$W = \Delta f \alpha^2 / 2 \quad (24)$$

The phase delay is  $(-2\pi/\lambda) \Delta f \alpha^2 / 2$  since defocus shortens the path length.

Thus a ray encountering both spherical aberration and defocus will be phase shifted by

$$\gamma = (2\pi/\lambda) (C_s \alpha^4 / 4 - \Delta f \alpha^2 / 2) \quad (25)$$

This is the result obtained by Scherzer (1949). It is verified by the experimental results of Thon (1970),

who studied micrographs of amorphous carbon with an optical diffractometer. Krakow, Downing, and Siegel (1974) also worked with amorphous carbon and also verified this formula.

However, the equation is disputed by Heidenreich (1964), Appendix B, on the basis of a diagram such as Figure (3). The optical path difference  $W$  between the aberrated ray  $AVC$  and the paraxial ray  $AVD$  is from the geometry

$$\begin{aligned}
 VC - VD &= CD \sin \beta \\
 &= M C_s \alpha^3 \beta \\
 &= M C_s \alpha^3 \alpha/M \\
 &= C_s \alpha^4
 \end{aligned} \tag{26}$$

a factor of 4 larger than the previous result. Similarly, in Figure (4), the in-focus ray  $BVE$  has an extra distance

$$\begin{aligned}
 EF \sin \beta &= M \Delta f \alpha \beta \\
 &= M \Delta f \alpha \alpha/M \\
 &= \Delta f \alpha^2
 \end{aligned} \tag{27}$$

to travel. This result differs by a factor of 2 from that of Thon but also from that of Heidenreich. The combined phase delay is

$$\gamma = (2\pi/\lambda) (C_s \alpha^4 - \Delta f \alpha^2) . \quad (28)$$

Although this derivation is simpler than that of Equation (25), it is probably incorrect. As mentioned previously, Equation (25) has been verified by the results of Thon (1970) and of Krakow, Downing and Siegel (1974). Therefore the coefficients 1/4 and 1/2 will be used in this thesis. They are also widely accepted in the literature.

#### 2.4 Lattice Imaging, Phase Contrast and Optimum Defocus

Spherical aberration, although it limits the resolution, can be used to improve contrast. Consider a thin specimen in which only elastic scattering is important. If only the central beam is allowed to contribute to the image, the intensity would be essentially uniform. The scattered beams are all very weak and excluding them is not sufficient to produce noticeable contrast.

If the central beam and one diffracted beam are allowed to contribute to the image, then lattice fringes can be obtained. This can be shown mathematically by considering the image amplitude as the sum of two beams:

$$\psi = A \exp[i(\theta_0 + \gamma_0)] + B \exp[i(2\pi gx + \theta_g + \gamma_g)] \quad (29)$$

Here A is the amplitude of the central beam, B that of the diffracted beam. Their initial phases are  $\theta_0$  and  $\theta_g$ .  $\gamma_0$  and  $\gamma_g$  are the phase shifts due to spherical aberration and defocus. The reciprocal lattice vector of the diffracted beam,  $g$ , is in the x direction. Then the intensity in the image plane is:

$$I = \psi\psi^* = A^2 + B^2 + 2AB \cos(2\pi gx + \theta_g + \gamma_g - \theta_0 - \gamma_0)$$

Thus the image is a sinusoidal intensity variation of period  $1/g$ . The effect of the phase  $\chi = \theta_g + \gamma_g - \theta_0 - \gamma_0$  is to translate the interference pattern. This shows the dependence of fringe position on the focus. The phase  $\chi$  has no effect on the contrast in this case. Of course, this is a simplified analysis. The full theory takes into account the thickness of the specimen, the effect of absorption, the deviation from the Bragg angle, etc.

If the central beam and two weak symmetrical diffracted beams are transmitted, with the central beam on the optic axis, i.e.,  $\theta_0 = \gamma_0 = 0$ ,

$$\psi = A + B \exp[i(2\pi gx + \theta_g + \gamma_g)] + B \exp[i(2\pi gx + \theta_{-g} + \gamma_{-g})]$$

The amplitudes B ( $B \ll A$ ) of the diffracted beams are

assumed equal, as are their phase shifts:  $\theta_g = \theta_{-g}$ ,

$\gamma_g = \gamma_{-g}$ . Therefore

$$I = A^2 + 4B^2 \cos^2 2\pi g x + 4AB \cos 2\pi g x \cos(\theta_g + \gamma_g).$$

The image contrast contains a weak contribution with periodicity  $1/2g$ , and a stronger contribution of period  $1/g$ . The visibility of this stronger contribution is however controlled by the cosine of the phase shift,  $\chi = \theta_g + \gamma_g$ . This arrangement of a pair of symmetrical diffracted beams interacting with the central beam is called phase contrast. The foregoing analysis is found in Heidenreich (1964), page 138. Of course, one pair of diffracted beams does not add very much information to the image, so as many pairs as possible should be transmitted.

To produce phase contrast, the phase of the scattered beams must be shifted by  $\pi$  or some multiple thereof before they recombine with the central beam. Diffracted beams suffer a phase shift of approximately  $\pi/2$  on being scattered (Haine, 1961, page 78; see also Figure (5)), and additional shifting can be produced by spherical aberration and defocus. Equation (25), which calculates this phase shift, is plotted in Figure (6) for various values of defocus.

In general, contrast is maximized when the total phase shift of a scattered beam is some multiple of  $\pi$ , i.e.,

$$\chi = -\frac{1}{2}\pi + \gamma = -\frac{1}{2}\pi + (2\pi/\lambda) (\frac{1}{2}C_s \alpha^4 - \frac{1}{2}\Delta f \alpha^2) = n\pi \quad (30)$$

where  $n$  is an integer. Thus if a thin film of amorphous carbon is imaged, rays scattered at angles which phase shift them approximately  $n\pi$  will produce contrast, while those scattered near  $(2n-1)\pi/2$  will not produce contrast. But if rays at a certain angle do not produce contrast, then the spatial periodicity  $d = \lambda/\alpha$  associated with that angle will not appear in the image. The Fourier transform of such an image can be obtained with an optical diffractometer. (See Appendix I). The intensity pattern of the transform consists of concentric rings: dark rings alternating with lighter rings. The bright rings correspond to those angles which produced contrast; the dark rings correspond to those which did not. For an example see Figure (31).

With periodic specimens one deals with discrete beams and for maximum contrast the phase shift of a beam scattered at angle  $\alpha$  should also be as in Equation (30). But Equation (30) is equivalent to

$$\cos \chi = \cos[-\frac{1}{2}\pi + (2\pi/\lambda)(\frac{1}{2}C_s \alpha^4 - \Delta f \alpha^2/2)] = \pm 1 \quad (31)$$

Thus plotting  $\cos \chi$  ( or  $\sin \gamma$  ) against  $\alpha$  for fixed  $C_s$  and  $\Delta f$  is one way of determining at which angles beams will have the proper phase shift. Another way is to solve equation (30) for  $\alpha$ :

$$\alpha^2 = \frac{\Delta f \pm (\Delta f^2 + C_s (2n+1)\lambda)^{0.5}}{C_s}$$

Using  $d = \lambda/\alpha$ , this becomes

$$d = \lambda \left[ \frac{\Delta f}{C_s} \pm \left[ \frac{\Delta f^2}{C_s^2} + \frac{(2n+1)\lambda}{C_s} \right]^{0.5} \right]^{-0.5} \quad (32)$$

A plot of  $d$  as a function of defocus for  $C_s = 1.7$  mm is shown in Figure (7). The solid lines are lines of maximum contrast. Between these, lines of no contrast could be drawn. For a certain defocus it can easily be determined which reciprocal spatial frequencies are transmitted, which are not, and which are partially transmitted.

The phase contrast method is to have as many of the high-intensity diffracted beams as possible transmitted with maximum contrast, i.e. to have them phase shifted by  $n\pi$ . For different defocus values, the phase shifting at different angles varies. Examples are given in Figures (8) and (9). In most cases the optimum



conditions are obtained when the defocus is adjusted so that  $\cos \chi$  has a shape such as in Figure (8a). Then all beams falling between  $\alpha_1$  and  $\alpha_3$  will have a correct phase shift of approximately  $-\pi$ , and this region has its maximum extent. Any beams falling between  $\alpha_3$  and  $\alpha_4$  have the wrong phase shift: they will produce little contrast. Those falling between  $\alpha_4$  and  $\alpha_5$  have a phase shift of approximately  $n\pi$ , namely,  $n = 0$ , but it is opposite to that of the Region I beams. The contrast produced by the two regions will tend to cancel. Thus the beams of Region II should be excluded from the image. This is most conveniently done by inserting an objective aperture in the back focal plane which excludes all beams with  $\alpha > \alpha_3$ . Then only Region I beams contribute to the image, but the defocus has been chosen to maximize the extent of Region I. The defocus at which this optimum phase shifting occurs (called the Scherzer focus) depends on the value of the spherical aberration coefficient. This dependence can be found by the following argument:

When the defocus is optimum, the phase shift at the angle  $\alpha_2$  is approximately  $-5\pi/4$ . The point  $(\alpha_2, -5\pi/4)$  is then the minimum of the  $\chi(\alpha)$  function. Therefore set

$$d\chi/d\alpha = (2\pi/\lambda) (C_s \alpha^3 - \Delta f \alpha) = 0$$

then

$$\alpha^2 = \Delta f / C_s$$

Then set

$$-\pi/2 + (2\pi/\lambda) (\frac{1}{4} C_s \alpha^4 - \frac{1}{2} \Delta f \alpha^2) = -5\pi/4$$

$$C_s \Delta f^2 / 4 C_s^2 - \Delta f^2 / 2 C_s = -3\lambda/8$$

$$\Delta f^2 / C_s = 3\lambda/2$$

$$\Delta f = (1.5 \lambda C_s)^{0.5} \quad (33)$$

is the optimum defocus. See Figure (10). The result is the same if Equation (28) is used.

## 2.5 Transfer Theory

The imaging process in an electron microscope can be described mathematically by considering the transfer of information through successive stages of the microscope (Cowley, 1973; Lenz, 1970). The effect that a specimen has on the phase of an incident electron beam is given by the transmission function

$$t(x,y) = \exp(-i\sigma\phi(x,y)) \cong 1 - i\sigma\phi \quad (34)$$

for  $\sigma\phi$  small enough. Here the assumption is made that the incident wave is planar and has an amplitude of 1;

and that there is no absorption in the thin specimen.  $\phi(x,y)$  is the electrostatic potential of the specimen projected in a plane perpendicular to the electron beam.  $\sigma = \pi/V\lambda$  is a constant: a beam experiencing the potential  $\phi$  will be phase shifted by  $\sigma\phi$  with respect to a beam that does not.

The diffraction pattern that is formed in the back focal plane of the objective lens is the Fourier transform of the transmission function:

$$F(u,v) = \mathcal{F}(t(x,y)) = \iint t(x,y) \exp[-2\pi i(ux+vy)] dx dy$$

$$\text{or } F(u,v) = \delta(u,v) - i\sigma\phi(u,v) . \quad (35)$$

Ideally, the image corresponds to the intensity of the inverse Fourier transform of the diffraction pattern:

$$\psi(X,Y) = \mathcal{F}[F(u,v)] .$$

However, between the specimen and the image, the wave is modified by instrumental defects and conditions such as spherical aberration and defocus. The objective aperture also affects the function. Therefore

$$\psi(X,Y) = \mathcal{F}[F(u,v) \exp(i\gamma) A(u,v)] ,$$

where  $\gamma = (2\pi/\lambda)(\frac{1}{2}C_s \alpha^4 - \frac{1}{2}\Delta f \alpha^2)$  as before and  $A(u,v) =$

aperture function = 1 if the beam is transmitted; 0 if the beam is blocked. Therefore

$$\psi = \mathcal{F}[\delta(u,v)\exp(i0)A(0) - i\sigma\phi(u,v)\exp(i\gamma)A(u,v)]$$

$$\text{or } \psi(X,Y) = 1 - i\sigma \mathcal{F}[\phi(u,v)\exp(i\gamma)A(u,v)] . \quad (37)$$

If all scattered beams are phase shifted by  $\gamma = -\pi/2$ , and are transmitted, then

$$\psi(X,Y) = 1 - \sigma\phi(x,y) = 1 - \sigma\phi(-X/M, -Y/M) . \quad (38)$$

The intensity in the image plane is, however,

$$I = \psi\psi^* \cong 1 - 2\sigma\phi(x,y) , \quad (39)$$

neglecting higher order terms. Thus the image contrast in this approximation corresponds to the projected electrostatic potential of the specimen. Electron phase contrast microscopy attempts to make use of this relationship by phase shifting as many beams as possible by  $\pi/2$  and excluding all others.

## 2.6 Chromatic Aberration

It is also necessary to consider chromatic aberration because it tends to degrade the resolution. The foregoing calculations are the "ideal" achromatic approximations. Chromatic aberration occurs in an

electron microscope when the electron beam is not perfectly monochromatic. It cannot be completely eliminated because no practical achromatic magnetic lenses for high resolution work have been constructed to date. Also, the electron beam will never be perfectly monochromatic because the electrons have a small energy spread (about 1 eV) when they escape from the tip of the tungsten filament. They are then accelerated to 100 keV, so the energy spread is only  $1$  in  $10^5$ , but this can produce significant blurring if the lenses are not properly designed. Small instabilities in the accelerating voltage also contribute to the blurring.

When the electrons pass through the specimen, some are inelastically scattered, increasing the energy spread. High resolution work must be limited to thin specimens in order to minimize this effect. The magnetic field of the objective lens is not perfectly stable and can introduce time variations into the imaging. The magnitude of the chromatic aberration due to the instrument is gauged by a chromatic aberration constant  $C_c$ . A number of approaches are found in the literature for determining this coefficient.

Haine (1961), page 12, argues that the focal length of a weak magnetic lens is given by

$$f = KV/I^2 \quad (40)$$

where  $V$  is the relativistically corrected accelerating voltage<sup>1</sup>,  $I$  is the lens current, and  $K$  is a constant.

By differentiating, he gets

$$\Delta f = f(\Delta V/V - 2 \Delta I/I) . \quad (41)$$

To extend this to strong lenses, he replaces  $f$  by  $C_c$ :

$$\Delta f = C_c(\Delta V/V - 2 \Delta I/I) . \quad (42)$$

By using equation (13), this can be converted to

$$\Delta R = M \alpha C_c(\Delta V/V - 2 \Delta I/I)$$

or

$$\Delta r = \alpha C_c(\Delta V/V - 2 \Delta I/I) . \quad (43)$$

El-Kareh and El-Kareh (1970) on page 281 derive a similar formula:

$$\Delta r = \alpha C_c(\Delta V/V - 2 \Delta B/B) \quad (44)$$

where  $B$  is the maximum value of the magnetic field of the lens.  $\Delta B/B$  can be replaced by  $\Delta I/I$  if the lens is not operated in saturation. Equations (42) and (43)

---

<sup>1</sup> In lens equations relativistic effects are most conveniently taken into account by using a corrected accelerating voltage rather than the corrected electron mass.

imply that the circle of confusion due to chromatic aberration can be eliminated by adjusting the instability of the objective lens to compensate for the voltage instabilities. Although this is theoretically possible for a single electron, it is not possible for a group of electrons with a random energy spread.

Heinemann (1971) and Vorobev and Vyazigin (1967) state the formula as

$$\Delta f = C_c (\Delta V/V + 2 \Delta B/B) , \quad (45)$$

both without justification.

Hawkes (1972), page 68, gives the objective lens contribution to the chromatic aberration as

$$\Delta f = C_c \Delta V/V \quad (46)$$

without justification.

Finally, Heidenreich (1964) gives the equation as

$$\Delta r = C_c \alpha [(\Delta V/V)^2 + (2 \Delta I/I)^2]^{0.5} . \quad (47)$$

This apparently comes from statistical error theory, as derived, for example, in Squires (1968), chapter 4. Applying it to equation (40) gives

$$(\Delta f/f)^2 = (\Delta V/V)^2 + (2 \Delta I/I)^2 .$$

Extending to strong lenses:

$$\Delta f = C_c [\Delta V/V)^2 + (2 \Delta I/I)^2]^{0.5} . \quad (48)$$

This seems to be the most reasonable approach, since it assumes that the two effects are not correlated.



## CHAPTER 3

### EXPERIMENTAL PROCEDURE

#### 3.1 Specimens and Specimen Preparation

All the specimens used were mounted on copper grids which had been coated with a Formvar film and vacuum-evaporated with carbon. The Formvar film is produced by dipping a microscope slide in a solution of 0.125% by weight Formvar in chloroform, then breathing on it to create holes. When the film is floated off and mounted on grids, holes down to 0.05 micron diameter are found. These are useful for astigmatism correction in the microscope. The larger holes allow specimens to project over the edge and be studied without the interference of a substrate.

The main specimen used was BiOCl: bismuth oxychloride. This is a tetragonal crystal with  $c = 0.7347$  nm and  $a = 0.3883$  nm (Crystal Data Determinative Tables, 1973). A diagram of its structure is given in Figure (12). The heavy Bismuth atoms (atomic number 83) are 0.2746 nm apart. The BiOCl crystals were prepared by saturating a small amount (10 ml) of HCl acid with BiCl<sub>3</sub> (Turner, 1965). A drop of this solution in a small amount of distilled water gives a white precipitate of BiOCl crystals.

The heavier particles quickly settle, but the small, useful ones remain suspended indefinitely. A drop of this suspension on a holey carbon coated grid deposits the crystals. The small crystals are often platelike and thin. They tend to sit on the specimen grid with their c-axes approximately parallel to the optic axis, which is the preferred orientation. Under electron irradiation,  $\text{BiOCl}$  crystals do suffer damage, but they do not become amorphous, rather, they develop "patches" which seem to be thinner than the rest of the specimen. These can be seen in Figure (13).

Magnesium oxide crystals were also used extensively. They were prepared by the standard method of burning magnesium, immersing the ash in an ultrasonic bath, and depositing a drop on a prepared grid. The structure of  $\text{MgO}$  is the face-centered cubic structure of  $\text{NaCl}$ . The lattice parameter is  $a = 0.42117 \text{ nm}$  (CRC Handbook, 1972).

Other specimens examined include thin amorphous carbon films, partially graphitized carbon (lattice spacing  $0.34 \text{ nm}$ ), biotite, and muscovite. The thin amorphous carbon films were prepared by evaporating carbon on mica, floating the films off, and mounting them on grids. Biotite and muscovite are minerals

belonging to the mica group. They are monoclinic double-sheet silicates with unit cell axes of  $a = 0.530$  nm,  $b = 0.921$ ,  $c = 2.006$ ,  $\beta = 99^\circ 3'$  and  $a = 0.517$ ,  $b = 0.894$ ,  $c = 2.012$ ,  $\beta = 98^\circ 6'$ , respectively (Bragg, 1937).  $\beta$  is the angle between the  $a$  and  $c$  axes. The two substances are almost identical: the only difference is that muscovite has aluminum atoms binding its double sheets together, while in biotite Mg and Fe replace the Al. The specimens were supplied by Dr. Lambert of the Geology Department, University of Alberta.

### 3.2 Calibration

When attempting high resolution work on an electron microscope, the various parameters must be carefully controlled. Therefore a calibration of the instrument is important. A JEM-100B electron microscope was used in the normal transmission mode. A high resolution pole piece was substituted for the normal pole piece. The high resolution pole piece has a narrow bore and does not permit the use of a tilting stage. To obtain a crystal at a certain orientation, the specimen grid must be searched until one is found.

In order to find the best conditions for high resolution work, the calibration was done for a range of specimen heights within the objective lens. This was done using a z-stage: a specimen holder with which the specimen can be raised or lowered by a screw mechanism. The length of the specimen holder was measured to obtain an arbitrary parameter of specimen height. See Figure (11). The objective lens current for the in-focus specimen was also monitored with a Hewlett-Packard 3460B digital voltmeter. The voltmeter has an accuracy of  $\pm 0.008\%$ , a short term stability of  $\pm 0.004\%$ , and a long term stability of  $\pm 0.012\%$ , in the range in which it was used. The voltage was measured across the 1 ohm (nominal) reference resistor of the objective lens ammeter.

### 3.2.1 Magnification

Once all lenses are set to obtain highest magnification, only the objective lens current is adjusted to focus the image. The amount of objective lens current necessary to achieve this is different for different specimen heights. The magnification also changes and does not remain at the nominal value of 500000X. Therefore it was measured using lattice images of  $\text{BiOCl}$ . These were obtained by the standard

method of tilting the illumination so that the optic axis is midway between the central beam and one diffracted beam, in this case a (110) spot. The (110) interplanar spacing is 0.2746 nm. An optional method is to tilt the optic axis until it is equidistant from four spots such as the (000), (110), ( $1\bar{1}0$ ), and (200) spots, as in Figure (14). It is then possible to obtain perpendicular sets of (110) reflections as well as (200) fringes at 45° to them. The lattice images from both methods often extend for considerable distances as can be seen in Figures (13) and (15). The fringe spacing can therefore be measured extremely accurately with a travelling microscope.

The magnification, determined mainly from such measurements, is plotted against objective lens current in Figure (16), and against specimen height in Figure (17). The lattice image spacing on some micrographs was obtained indirectly by using an optical diffractometer (Appendix I). This instrument produces the Fourier transform of a micrograph, so the sinusoidal fringes produce two spots whose separation is inversely proportional to the fringe spacing. This method of obtaining the magnification, though not as accurate as the travelling microscope, is especially valuable when the lattice images are faint.

The data shows scatter mainly because the fringe spacing can vary if the diffracted beam is not in the exact Bragg condition, as was mentioned in the introduction. For example, the two data points in boxes in Figures (16) and (17), at a current of 0.75043 Amp (height 5.24833 cm) were taken from the same micrograph - two different regions of the same specimen. The fringe spacing changed continuously from one end of the specimen to the other. Other reasons for the scatter of the data in Figure (16) are:

1. The accuracy of the resistor across which the lens current is measured is limited. Its resistance will fluctuate slightly because of temperature variations.
2. The objective lens has hysteresis. As a result various values of the objective lens current may correspond to the same magnetic field strength of the lens, and vice versa. The magnetic field, after all, does the imaging.

On the other hand, using the length of the specimen holder as a measure of the magnetic field when the image is focussed also has drawbacks:

1. The specimens sit at different heights on the specimen grid.

2. The specimen grid may be uneven.
3. The specimen holder may not sit at exactly the same height each time it is inserted (sometimes due to dust in the microscope column).
4. The mechanism of the z-stage, together with the microscope tilt controls used to manipulate it, has a certain inaccuracy.
5. The length of the specimen holder is difficult to measure precisely.

The total uncertainty, obtained from the graphs, is about  $\pm 2\%$  in both cases. It was decided to use the objective lens current as the magnetic field strength parameter for all calibrations, since the length measurements are restricted to one specimen holder.

### 3.2.2 Camera Length

The camera length also depends on the magnetic field needed to focus the image. It was measured in order to be able to identify the various diffracted beams that were obtained. The camera length setting given as 80 cm by the manufacturer was calibrated by using the diffraction patterns of known crystals, mainly  $\text{BiOCl}$ . The objective lens was set for highest magnification. The results are plotted in Figure (18). Again the error is about  $\pm 2\%$ .

### 3.2.3 Defocus Dependence on Current Change

The image contrast in high resolution work depends critically on the focus of the microscope. Thus it is necessary to have some means of monitoring the change of focus when the knobs on the instrument are manipulated. One method of obtaining such a calibration is to actually change the specimen height a small known amount and to record the different lens currents necessary to focus the specimen at these heights. The change in focus (i.e., the change in height) can then be found as a function of the current change. Specimen height is plotted against objective lens current in Figure (19). The slope of the graph is the required dependence, i.e.,  $\partial f/\partial I$ . However, the slope is difficult to judge because of the scatter of the data. One way to approximate the slope is to fit a regression curve to the points and to use the slope of the fitted curve. This is the dashed line in Figure (20). Another way is to use the slopes obtained from a series of data points taken in succession during a single session on the microscope. The data points in squares in Figure (19) are such a sequence. The corresponding slopes are also plotted as squares in Figure (20). Such data from other sequences are plotted as triangles.



Since one is finding small differences, such data has a large error. Therefore another method was tried. It is due to Heinemann (1971) and involves measuring the lateral shift in the image plane of an off-axis beam as the objective lens current is changed. This shift  $\Delta R/\Delta I$  is related to the focus change by equation (19):

$$\Delta R = M \Delta f \alpha$$

$$\text{or } \Delta f = \Delta R/M\alpha \quad (49)$$

Therefore

$$\Delta f(\Delta I) = \Delta R(\Delta I)/M\alpha \quad (50)$$

$\Delta R$  was measured by using the various diffracted beams of MgO crystals. Photographic plates were doubly exposed to one dark field image at two slightly different lens current settings. Such micrographs are shown in Figure (21). The accuracy is limited by the fuzziness of the image which makes it difficult to measure the shift precisely. However, defocussing the illumination helps to sharpen the images. The central beam image was voltage centered before taking such calibration photographs. But even so, the central beam image often moved slightly on changing the objective lens current. This was taken into account in the calculations.

The results of the calculations are plotted as circles on the same graph (Figure (20)) as the values obtained by the previous method. It can be seen that the Heinemann method produces results with less scatter. The solid line is a least squares fit to the circled data. However, comparing the two sets of data suggests that a systematic error is involved in one or the other of the two methods.

Heinemann reports an error of  $\pm 2\%$  for his data, whereas the circled data in Figure (20) has an accuracy of about  $\pm 5\%$ . However, Heinemann used two symmetrical diffracted images for his calibration. No such properly oriented MgO crystals were found, and the high resolution pole piece that was used does not allow tilting.

#### 3.2.4 Defocus Per Click

The objective lens current is controlled by 5 click-type knobs. A click in either direction slides contacts across banks of resistors to the next contact points. It is useful to know how much the focus changes when any knob is adjusted by one click. To find this it is necessary to know the change in objective lens current per click of each knob. These values change with increasing lens current, so again graphs are necessary (Figures (22) to (25)).

The change in lens current per click of the finest knob is too small to be measured: even 22 such clicks (the maximum) change the lens current by only about .00003 Amp. But that is on the limit of the stability of the digital voltmeter. A solution to this problem was found when it was noticed that the general shape of the graphs is the same for all the other knobs; and furthermore, that the ratios between them are constant. A network analysis of the objective lens focussing circuit confirmed that this should be so. See Appendix II. A manual check of the values of the resistors involved made it possible to calculate these ratios. (The resistor values on the circuit diagram supplied by the manufacturer were incorrect.) The calculated ratios, which agreed with the available empirical ratios, are given below:

Ratios of the lens current change per click

$$\frac{\text{medium knob}}{\text{fine medium knob}} = 12.66$$

$$\frac{\text{fine medium knob}}{\text{second finest knob}} = 17.73$$

$$\frac{\text{second finest knob}}{\text{finest knob}} = 16.32$$

Therefore the "strength" of the finest knob, as a fraction of the second finest, could be calculated with some confidence.

The lens current change per click graphs were then combined with the  $\Delta R(\Delta I)$  graph obtained by the Heinemann method to give a focus change per click graph for each knob. These are plotted in Figures (26) to (29). It is interesting to note that, except for the discontinuity, the defocus values per click are constant, within the error limits. The error is estimated to be  $\pm 10\%$ . In the range of interest (around .77 Amps) the defocus values per click are:

medium knob: 12.3 microns

fine medium knob: .97 microns

second finest knob: 55 nm

finest knob: 3.34 nm

The nominal values supplied by the manufacturer are, respectively, 14.4 microns, 1.2 microns, 76 nm, and 4.4 nm.

### 3.2.5 Chromatic Aberration

From equation (48) we have

$$C_c = \Delta f [(\Delta V/V)^2 + (2 \Delta I/I)^2]^{-0.5}$$

From this we get:

$$C_c < \Delta f / (2 \Delta I/I) = 0.5 \Delta f I / \Delta I \quad (51)$$

Thus the amount of defocus for a small current change

is a measure of the upper limit of the chromatic aberration of the objective lens. It can be obtained by multiplying the solid line of Figure (20) by  $I/2$ . The result is shown in Figure (30). As can be seen, the chromatic aberration constant is less than 1.1 nm. The radius of the confusion circle in the object plane due to chromatic aberration of the objective lens can now be estimated. Since our microscope is well stabilized against voltage and current fluctuations, and since the lens probably runs with some saturation at high currents,  $\Delta V/V$  can be taken as  $10^{-5}$  and  $\Delta I/I$  as  $10^{-6}$ . Using equation (47) and taking  $\alpha = 0.01$  radians, gives  $\Delta r < .11$  nm. This is much less than the hoped for resolution of about .25 nm, and can be neglected.

### 3.2.6 Spherical Aberration

The most important constant that must be found is the spherical aberration coefficient. Various methods were tried in an effort to obtain an accurate value of it.

The image contrast of a thin carbon film depends on the spherical aberration and the defocus, as was shown in section 2.4. Thus a series of photographs of such a film, taken at small defocus steps near the

paraxial focus, carries information about the magnitude of both the spherical aberration and the defocus. In each micrograph the spatial frequencies that are suppressed correspond to scattering angles  $\alpha$  such that

$$\chi = -\frac{1}{2}\pi + (2\pi/\lambda) (\frac{1}{4}C_s \alpha^4 - \frac{1}{2} \Delta f \alpha^2) = (2n-1)\pi/2$$

$$\text{or } \frac{1}{2}C_s \alpha^4 - \Delta f \alpha^2 = n\lambda. \quad (52)$$

The value of  $\alpha$  for  $n = -1$  can be found from the Fourier transform of a micrograph. From Appendix I, the radius  $q$  of the first dark ring of the diffractogram is related to the corresponding scattering angles  $\alpha$  by

$$\alpha = \lambda_1 M q / \lambda_2 L = cq. \quad (53)$$

If the amount of defocus from the Gaussian image plane is known, a value of  $C_s$  can be calculated from

$$C_s = 2\alpha^{-2} (\Delta f - \lambda/\alpha^2) = 2(\Delta f - \lambda/c^2 q^2) / c^2 q^2. \quad (54)$$

It is found that the result of the calculation fluctuates widely because it is very sensitive to the value of  $q$ . In practice the rings are fuzzy (see Figure (31)) and cannot be measured accurately enough to give a reliable value for  $C_s$ .

If the defocus is not known, or if it is difficult to estimate the Gaussian focus, then the defocus can in theory be found from two carbon micrographs

separated by a small known defocus step  $\epsilon$ . (This can be easily monitored once defocus has been calibrated as a function of lens current.) An equation can be set up for each micrograph:

$$\frac{1}{2}C_s \alpha_1^4 - \Delta f \alpha_1^2 = -\lambda \quad (55)$$

$$\frac{1}{2}C_s \alpha_2^4 - (\Delta f + \epsilon) \alpha_2^2 = -\lambda.$$

By solving to eliminate  $C_s$ , an expression for  $\Delta f$  can be found. Unfortunately, the results are again unreliable because  $q$  cannot be measured precisely. Solving to eliminate  $\Delta f$  from equations (55) produces widely fluctuating values of  $C_s$  also.

Heinemann (1971) gives a method of determining spherical aberration which he found to be accurate to 5%. It involves the fact that the axial image and any diffracted beam of a periodic specimen do not coincide in the Gaussian image plane because of spherical aberration. For defocus  $\Delta f$ , the separation of the axial image and a certain image diffracted at angle  $\alpha$  is

$$\Delta R = M C_s \alpha^3 - M \Delta f \alpha. \quad (56)$$

(Assuming that all astigmatism has been corrected.)

The amount of defocus necessary to make the two images coincide, i.e., make  $\Delta R = 0$ , is

$$\Delta f = C_s \alpha^2 . \quad (57)$$

If the amount of defocus necessary is measured for a known dark field image,  $C_s$  can be calculated. But once the defocus is calibrated as a function of current change, it can easily be monitored with the digital voltmeter. The results of such measurements using MgO crystals are plotted as triangles in Figure (32).

Another method used by Hall (1949) was also tried. For exact paraxial focus (i.e.,  $\Delta f = 0$ ), equation (46) becomes

$$\Delta R = M C_s \alpha^3 . \quad (58)$$

Thus a knowledge of  $\alpha = 2\theta_b$  and of  $M$ , and a measurement of  $\Delta R$  at Gaussian focus, enables one to calculate  $C_s$ . Gaussian focus is estimated by the absence of Fresnel fringes in the direction which the diffracted image moves. The magnification has been calibrated and  $\alpha$  is found from the diffraction patterns. Examples of such measurements are seen in Figure (33). The data obtained by this method are plotted as circles in Figure (32). Magnesium oxide crystals were used because of their relatively sharp diffraction images.

One problem encountered was that the magnitude of the separation  $\Delta R$  was affected by the adjustment of the condenser lens. With the illumination defocussed,



the separation was sometimes observed to change as the illumination was moved across the specimen. With the illumination focussed the effect was not observed. However, it probably affected the separation and is one reason for the scatter of the data points. It also affects the measurements by the previous method. The scatter is larger for large objective lens currents, when the divergence of the illumination is high. Another source of error was the difficulty of judging the separation on the developed micrographs. From the graph, the data has an error range of approximately  $\pm 10\%$ . As can be seen, the spherical aberration is not the same at all objective lens currents required for focus at different specimen heights, but decreases at higher lens excitations.

## CHAPTER 4

### DISCUSSION

Once the instrument has been calibrated, the best imaging conditions must be selected. The most important parameter to consider is the spherical aberration.

For the JEM-100B, the manufacturer supplies a value for the spherical aberration coefficient of 1.4 mm. This is for the high resolution pole piece when it is used with a standard specimen holder. However, when a specimen held in a standard holder is focussed, the objective lens current reads about .715 Amp. From Figure (32) it is seen that for a current of .715 Amp, the spherical aberration is actually about 1.9 mm. To obtain a smaller value, one must go to higher currents - pushing the specimen farther towards the center of the objective lens. This increases the objective lens prefield - the part of the objective lens magnetic field that comes before the specimen. A large prefield causes the divergence of the illuminating beam to be very large at the specimen. That is not acceptable for high resolution work because it invalidates the projected potential approximation which assumes that the illuminating

radiation is planar. Defocussing the illumination does improve the divergence, but it also reduces the brightness of the image considerably. Setting the objective lens current to about .77 Amp keeps the divergence low while  $C_s$  decreases a little to about 1.7 mm. This was selected as the optimum height for high resolution work.

The transfer characteristics of the microscope for  $C_s = 1.7$  mm and optimum defocus of 97.1 nm are described by  $\cos \chi$  as in Figure (8a). In order to make use of the projected potential approximation, as many beams as possible should fall in Region I, and an objective aperture should be used to eliminate any beams with scattering angles greater than  $\alpha_3 = 0.010$  radians. Alternately, if some beams fall in Region I and some in Region III, but none between, then a larger objective aperture excluding only  $\alpha > \alpha_7 = 0.0126$  can be used.

For BiOCl the smallest scattering angles are  $\alpha_{110} = 0.0135$  and  $\alpha_{200} = 0.01906$ . Not even the least deflected beams will fit into Region I. Quite obviously, this makes the optimum defocus useless for obtaining structural information about BiOCl. Even for a spherical aberration coefficient as low as 1.0 mm, Region I is still too small, as can be seen in Figure (8b). An alternate approach is to try some

other defocus than the Scherzer focus. For  $\Delta f = 186$  nm and  $C_s = 1.7$  mm the transfer characteristics are as in Figure (9a). The idea is to have the diffracted beams in the region  $.0078 < \alpha < .0125$  radians where they would have a phase shift of approximately  $n\pi$ .

Such regions occur for

$$\Delta f = (\lambda C_s (2\ell + 1.5))^{0.5}, \ell \text{ an integer.} \quad (59)$$

They occur at larger angles for successively larger defocus values. However, they also become successively narrower at the larger angles. It can be seen that such a defocus will not work for BiOCl beams: the region is already too narrow at this defocus. A lower  $C_s$  value of 1.0 mm would give wider regions, as in Figure (9b), but they are still not wide enough.

The sheet silicates, biotite and muscovite, were also briefly examined. It was found that electron irradiation easily damages biotite. It becomes amorphous in less than five minutes even at low magnifications.

Muscovite, however, did not damage quickly, except for very thin specimens. Its lowest order beams, when in the  $[001]$  orientation, are  $\alpha_{020} = 0.00820$ ,  $\alpha_{110} = 0.00827$ ,  $\alpha_{200} = 0.01435$ , and  $\alpha_{130} = 0.0142$ . If only the (020) and (110) spots as well as the

central spot are transmitted, then a pattern of 3-fold crossed lattice fringes can be obtained, as in Figure (34). Such a pattern does reflect the basic periodicities of muscovite structure, but not enough beams contribute to the image to give one-to-one structural information. Also, the defocus need not be optimum to obtain such an image. Examining other focus values (for example, Figure (9b)) to check if they provide proper phase shifts for more than six diffracted beams leads to a negative result. Even with this specimen, the unit cell is too small to be able to properly phase shift enough beams to obtain useful structural information. High resolution microscopy is limited to materials with large unit cells until lenses with very little spherical aberration become available.

Edge on views of the sheet silicates were also found (Figure (35)). However, both biotite and muscovite quickly became amorphous when viewed in this position. It was concluded that this quick damage and not having any control over the orientation, makes any detailed interpretation questionable.

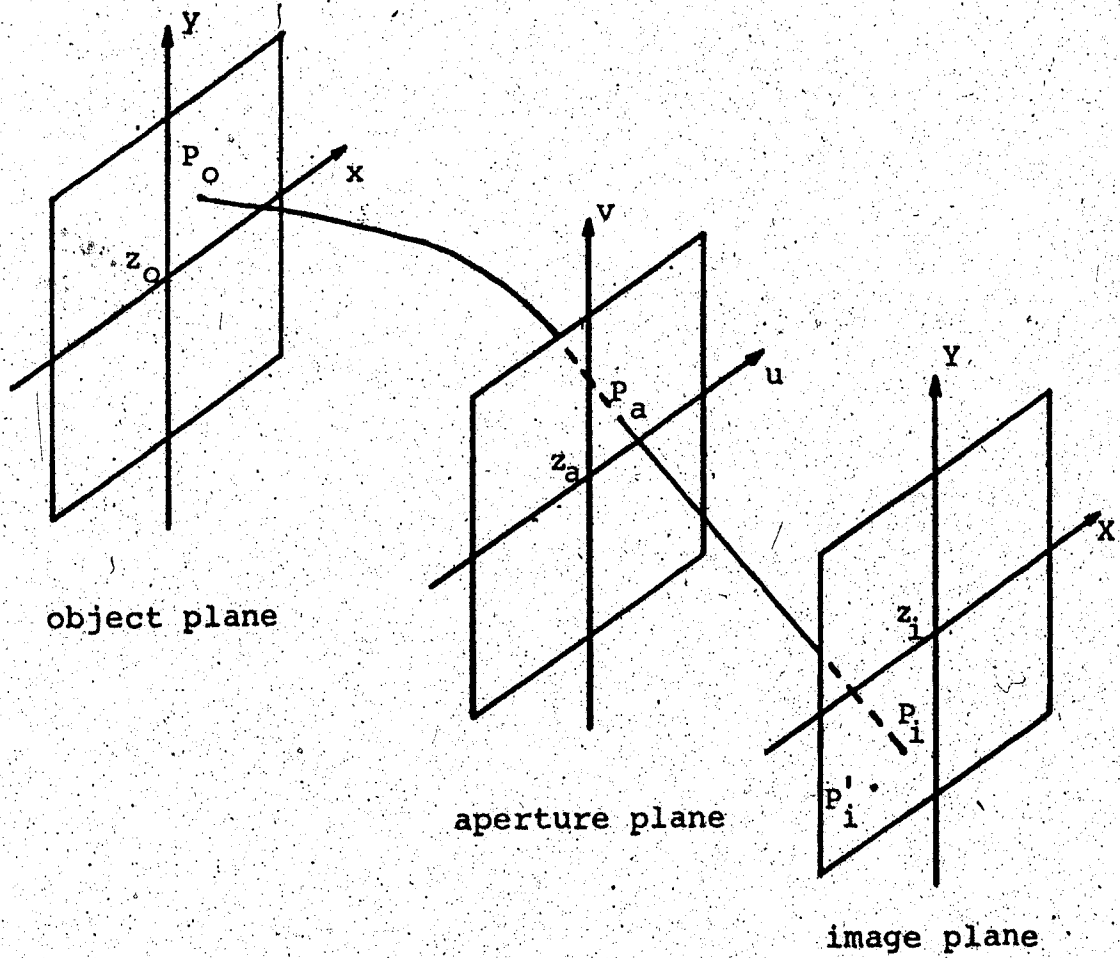


Figure (1) A rotationally symmetric optical system with mutually parallel rectangular Cartesian coordinates.

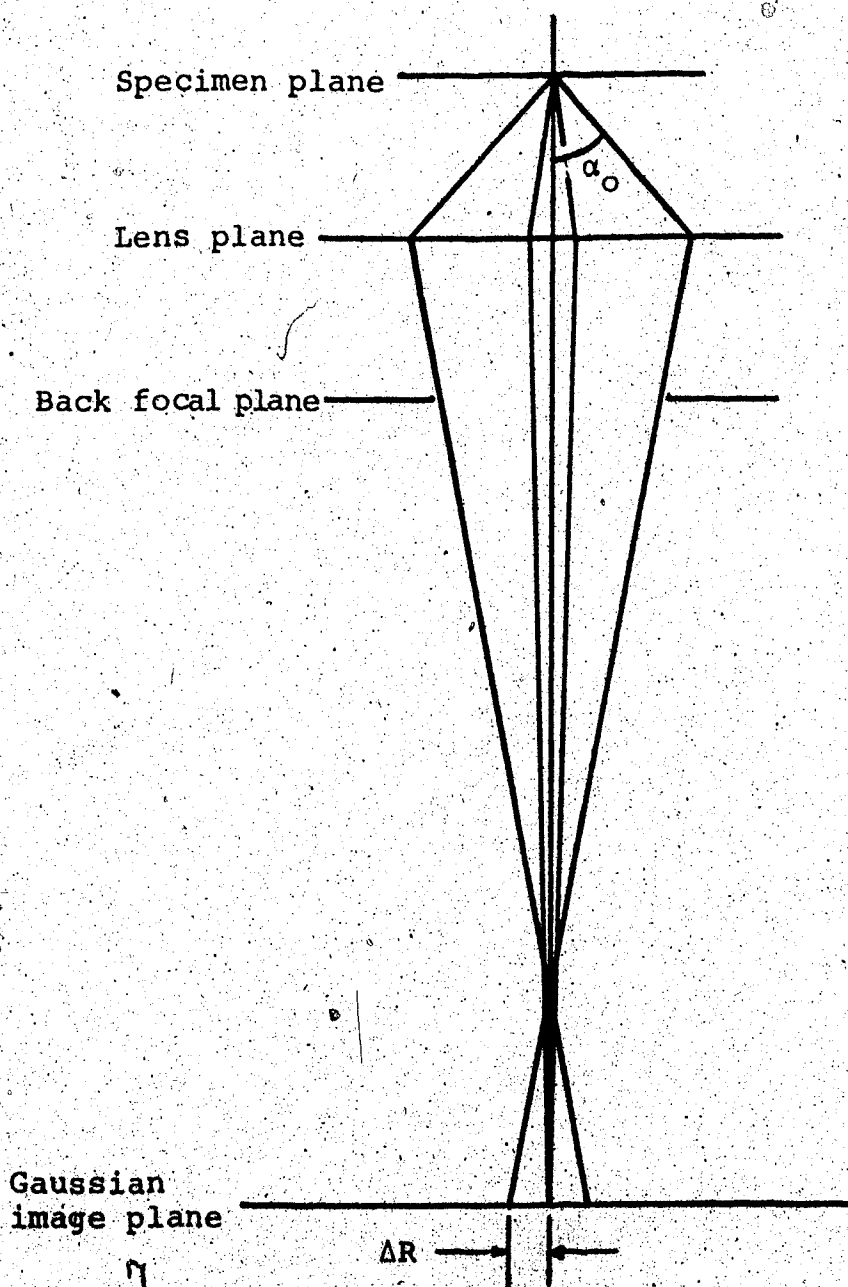


Figure (2) Spherical aberration causes the lens to deflect rays that are scattered at 'large' angles more strongly than the Gaussian approximation would have them deflected. The correctly deflected paraxial rays focus at the Gaussian image plane, while the aberrated rays form a circle of confusion of radius  $\Delta R = C_s \alpha_0^3$  in this plane.  $\alpha_0$  is the largest scattering angle that is allowed to pass through the objective aperture in the back focal plane.

Figure(3) The path of a ray AVC which encounters spherical aberration is longer than that of its paraxial approximation AVD.

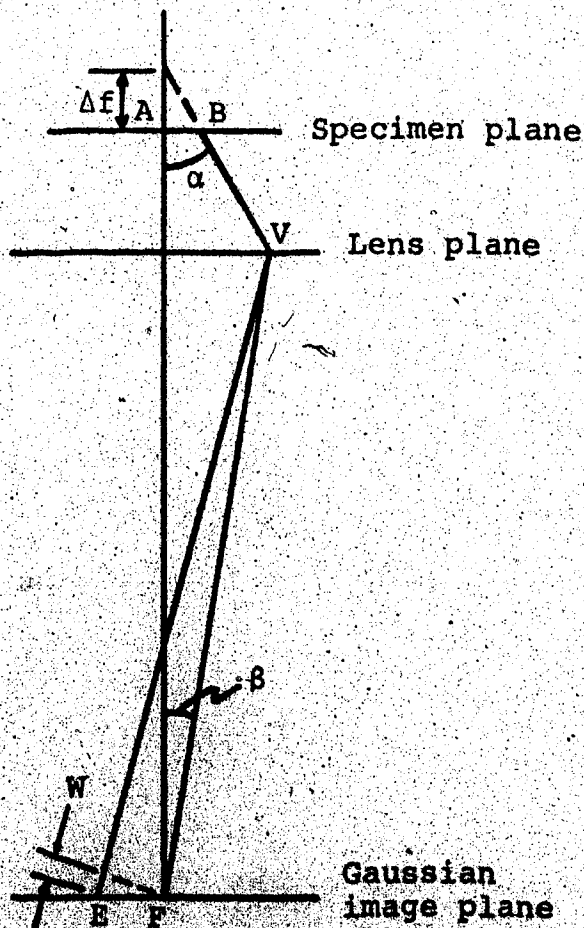
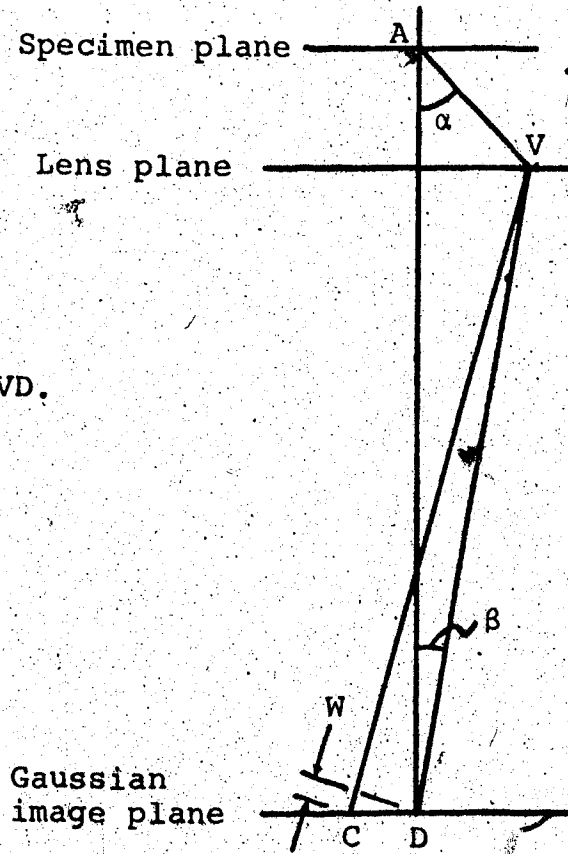


Figure (4) Defocussing advances the phase of a ray. An infocus paraxial ray takes the path BVE. When an amount of defocus  $\Delta f$  is introduced, the ray takes the path BVF, thereby shortening the distance it must travel.



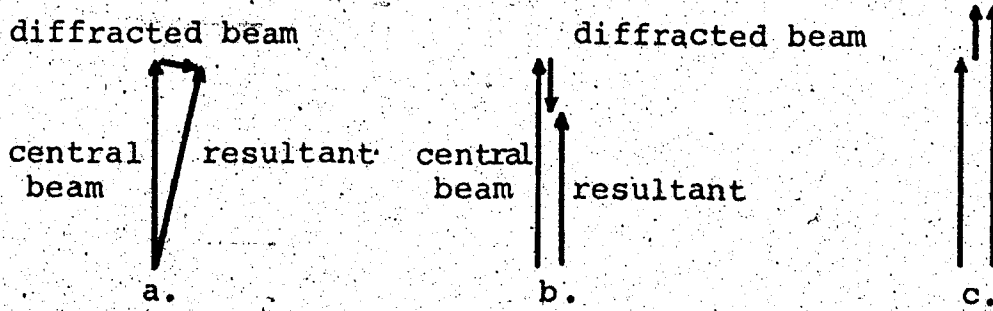


Figure (5) If an incident beam is phase shifted by a small angle, leaving its amplitude unchanged, as in a), the resultant is the sum of the original beam plus a diffracted beam with its phase shifted by approximately  $90^\circ$  with respect to the incident beam. The resultant will produce little contrast because it differs very little from the incident beam. But if the diffracted beam is phase shifted by  $180^\circ$ , as in b), or by  $0^\circ$ , as in c), the amplitude is changed quite appreciably.

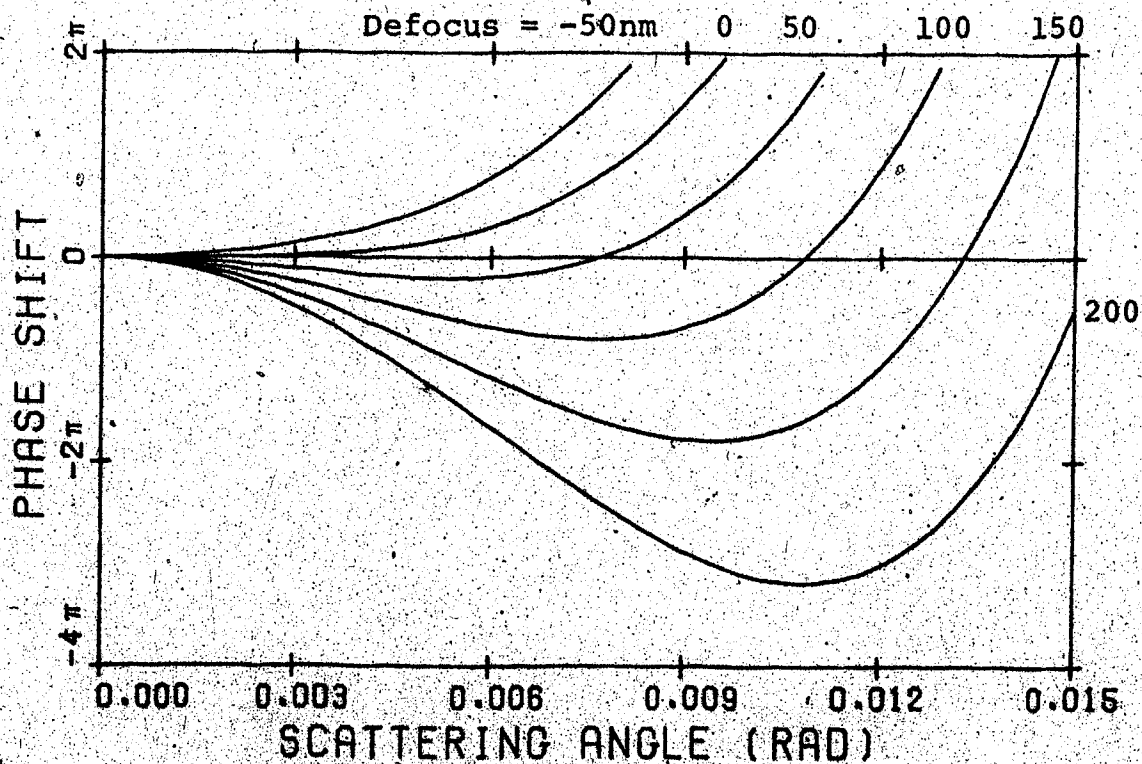


Figure (6) The phase shift due to spherical aberration and defocussing for  $C_s = 1.7 \text{ mm}$ ,  $\lambda = 0.037 \text{ nm}$ , and various defocus values.

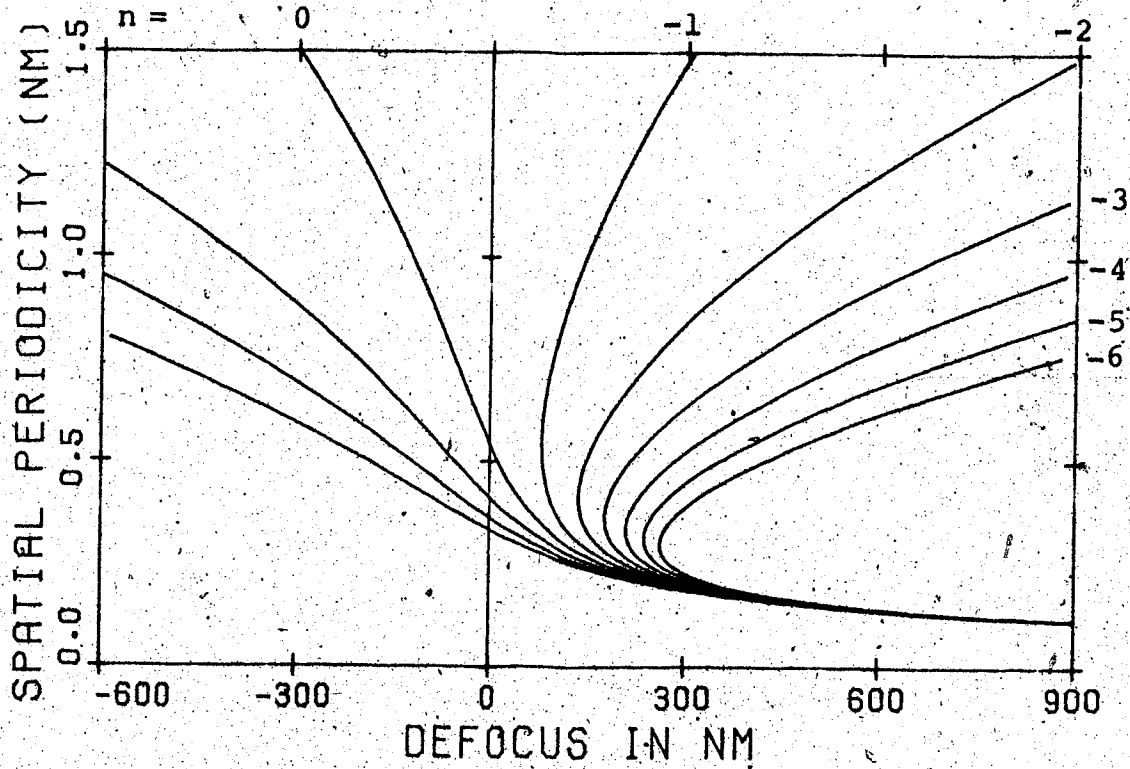


Figure (7) The transmitted spatial periodicities as a function of defocus for  $C_s = 1.7$  mm and  $\lambda = .0037$  nm. The curves represent phase shifts of  $n\pi$ .

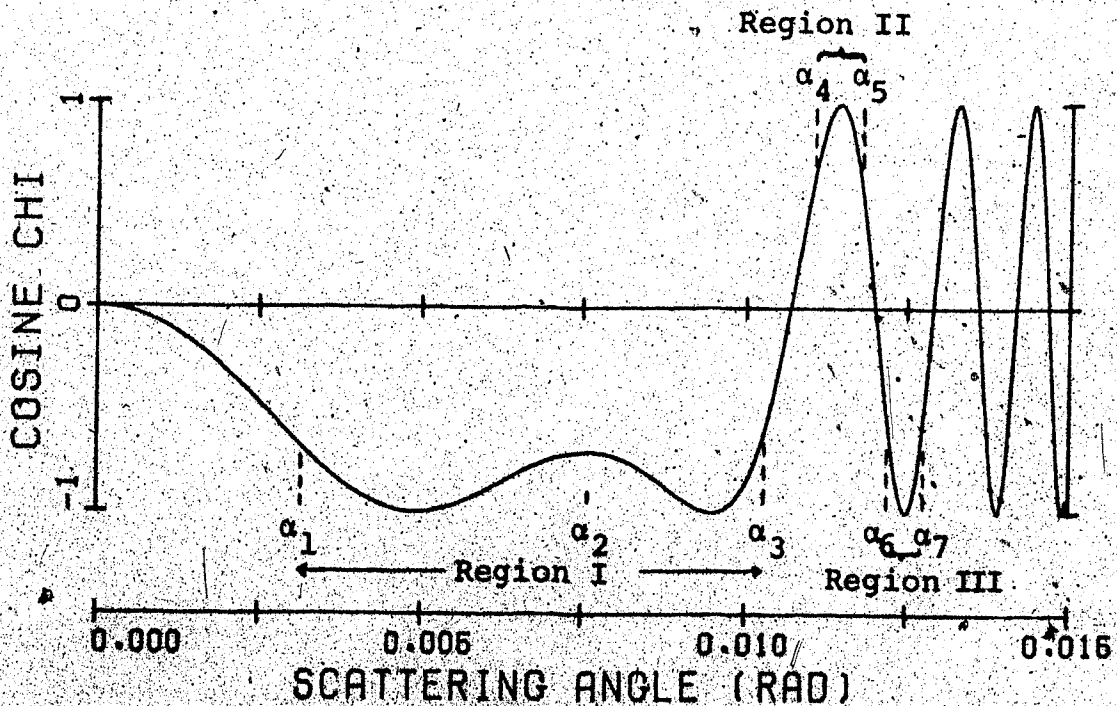


Figure (8a) The cosine of the total phase shift as a function of the scattering angle for optimum defocus of 97.1 nm,  $C_s = 1.7$  mm,  $\lambda = .0037$  nm.

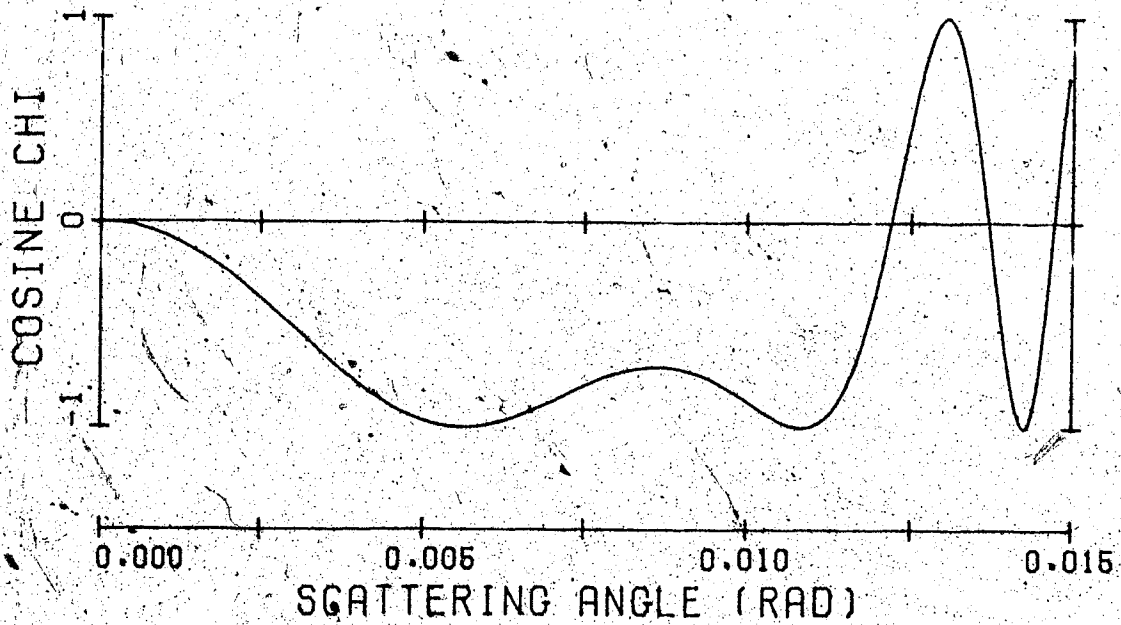


Figure (8b) The transfer function for  $C_s = 1.0$  mm and optimum defocus of 74.5 nm.

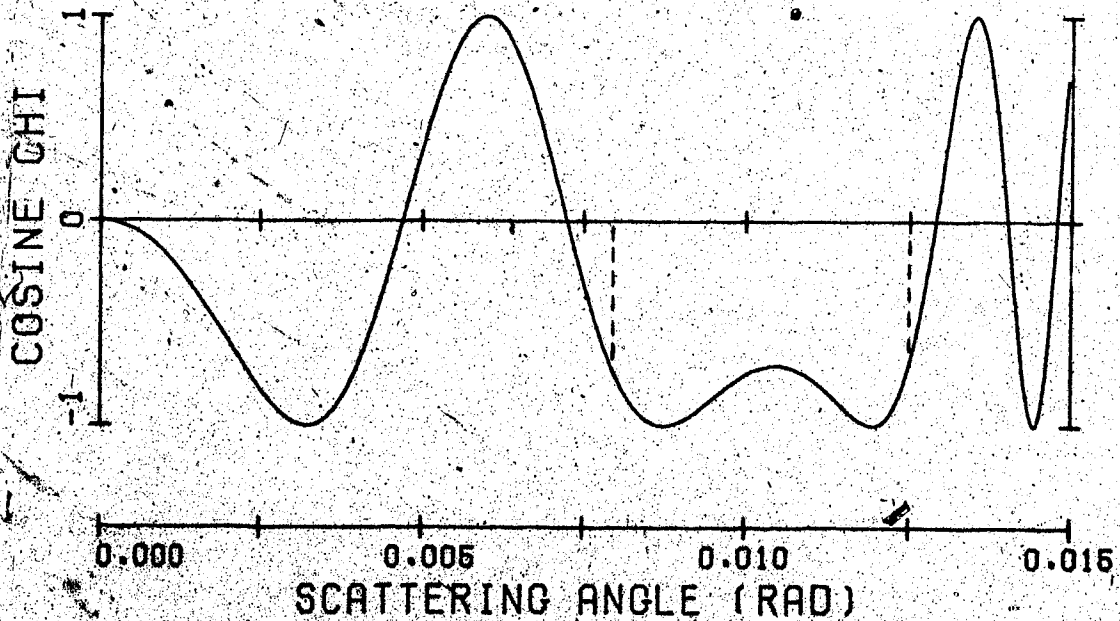


Figure (9a) The transfer function at a defocus of 186 nm and  $C_s = 7$  mm,  $\lambda = .0037$  nm.

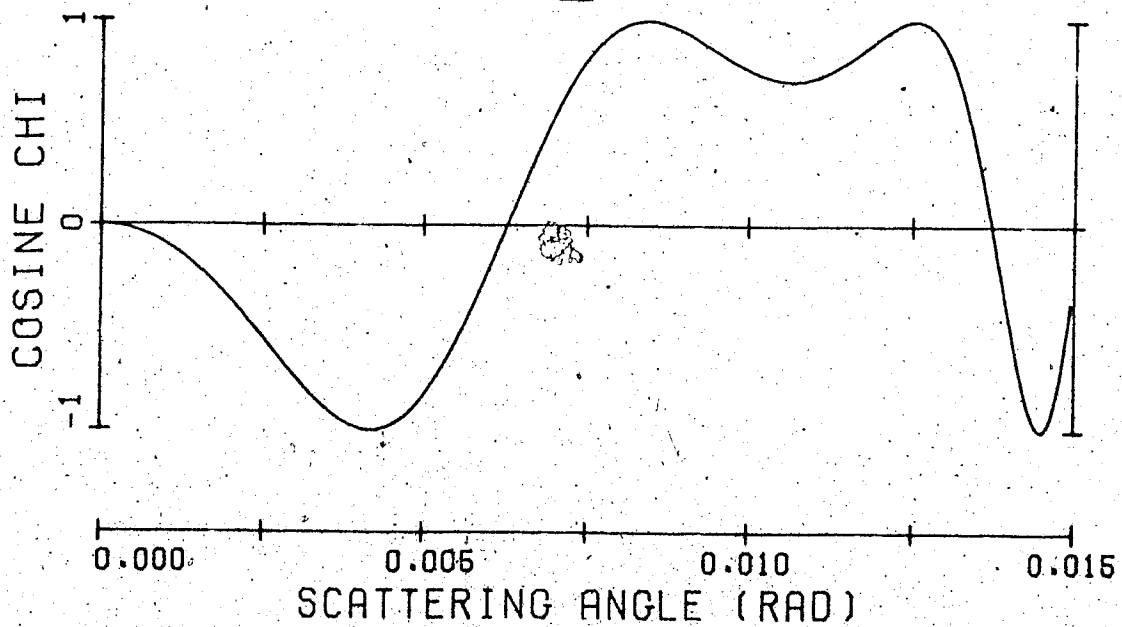


Figure (9b) The transfer function at a defocus of 113.8 nm.  $C_s = 1.0$  mm,  $\lambda = .0037$  nm.

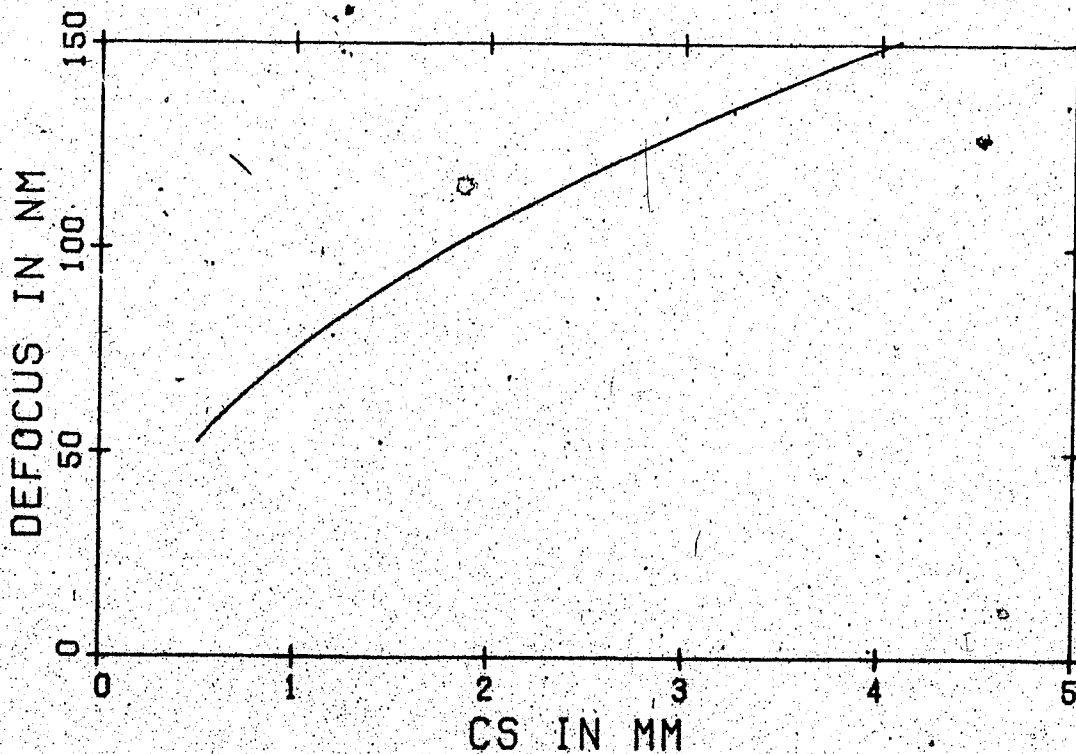


Figure (10) The optimum defocus for high resolution as a function of the spherical aberration coefficient of the objective lens.  $\lambda = .0037$  nm.

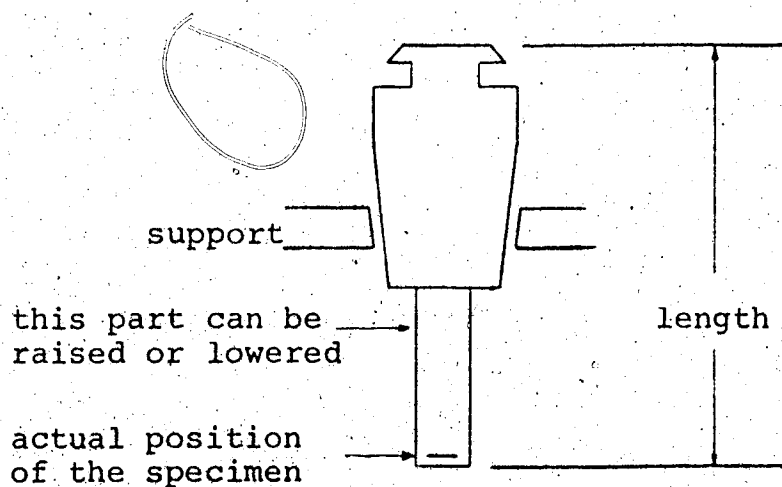


Figure (11) The z-stage as it is positioned in the microscope column. The length was used as an arbitrary parameter of specimen height.

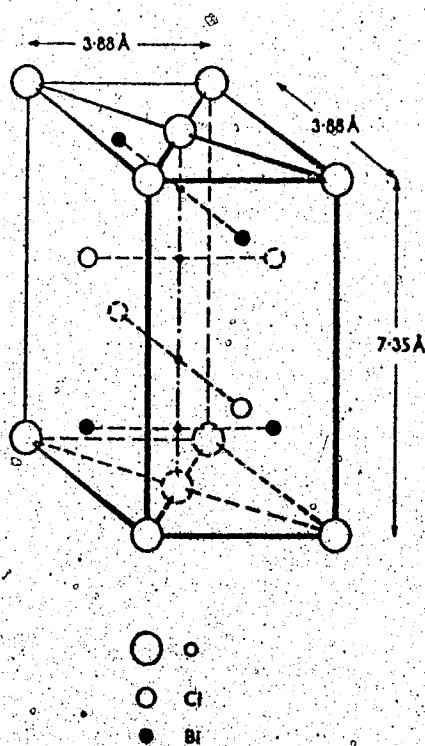


Figure (12) The structure of BiOCl after Cowley and Kuwabara (1962).

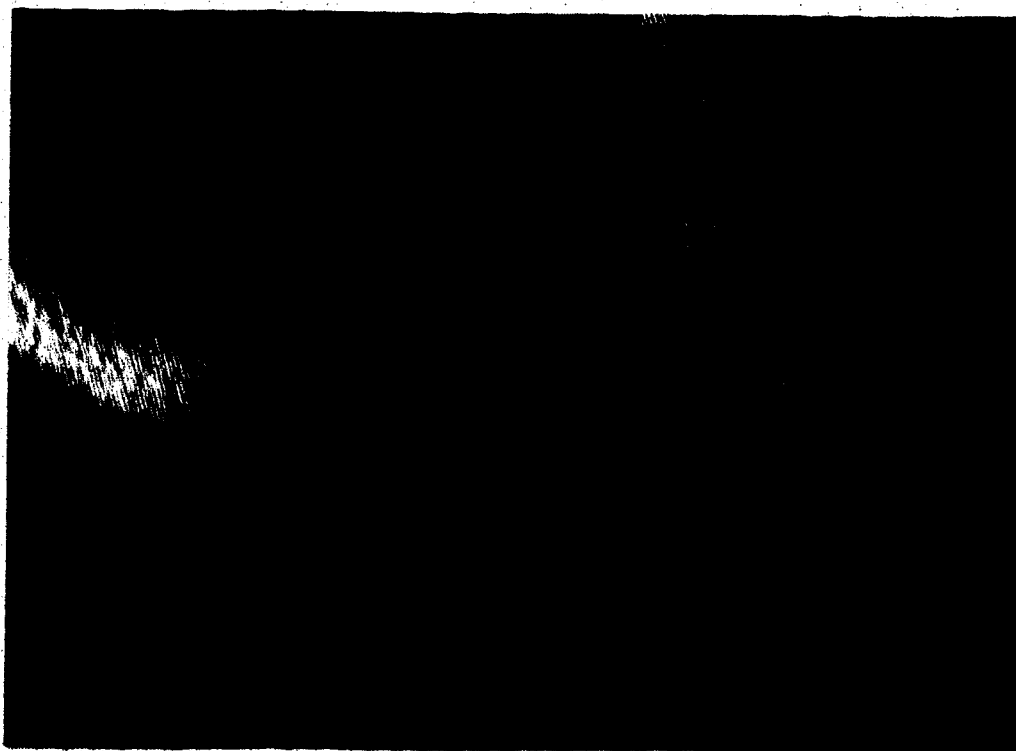


Figure (13) Lattice images of (110) BiOCl planes showing a spacing of 0.2745 nm.

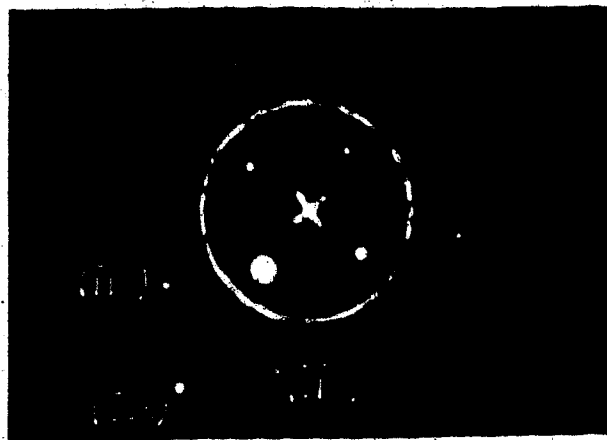


Figure (14) The  $(hk0)$  electron diffraction pattern of  $\text{BiOCl}$  showing the position of the objective aperture and the optic axis for obtaining crossed lattice fringes.

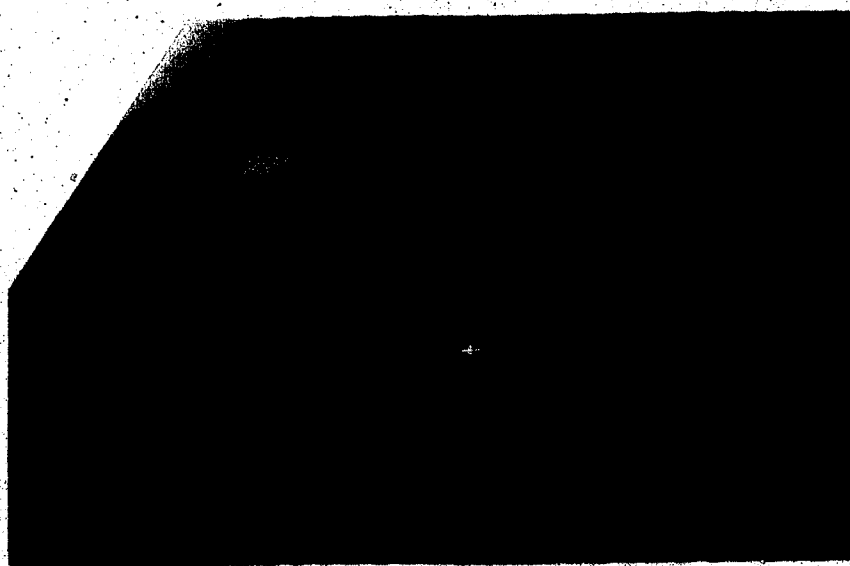


Figure (15) Crossed lattice images of  $\text{BiOCl}$  showing the  $(110)$  spacing of 0.2746 nm as well as the  $(200)$  spacing of 0.194 nm.

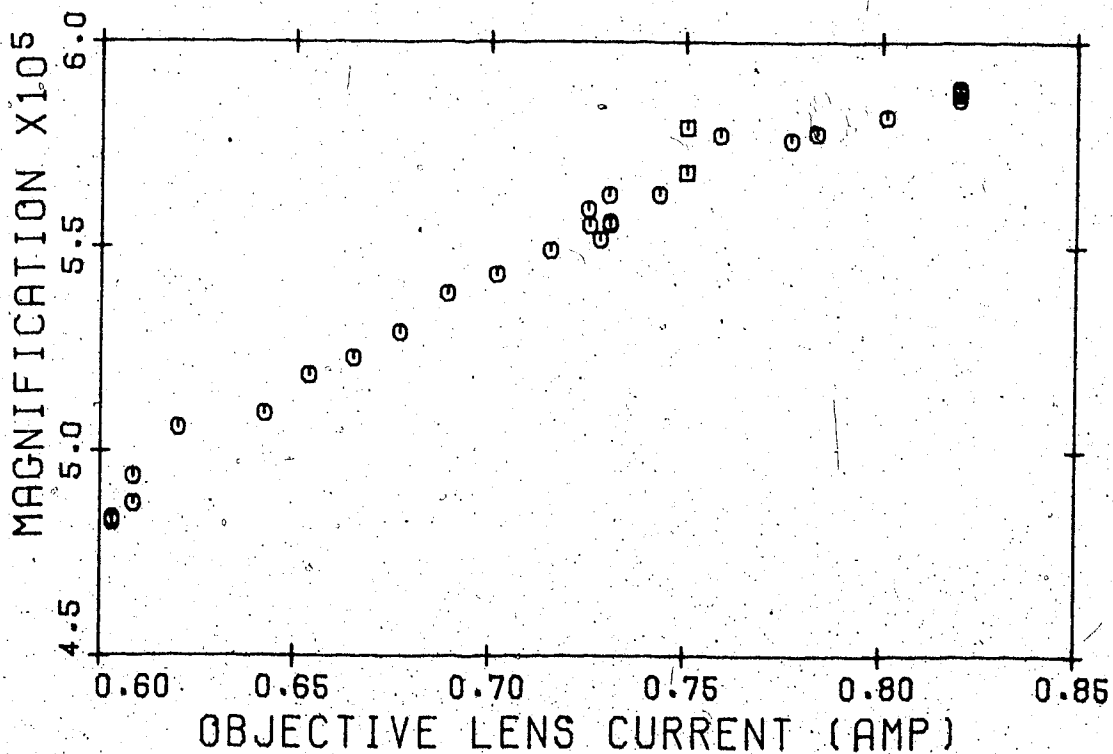


Figure (16) The magnification (nominally 500000) as a function of the objective lens current.

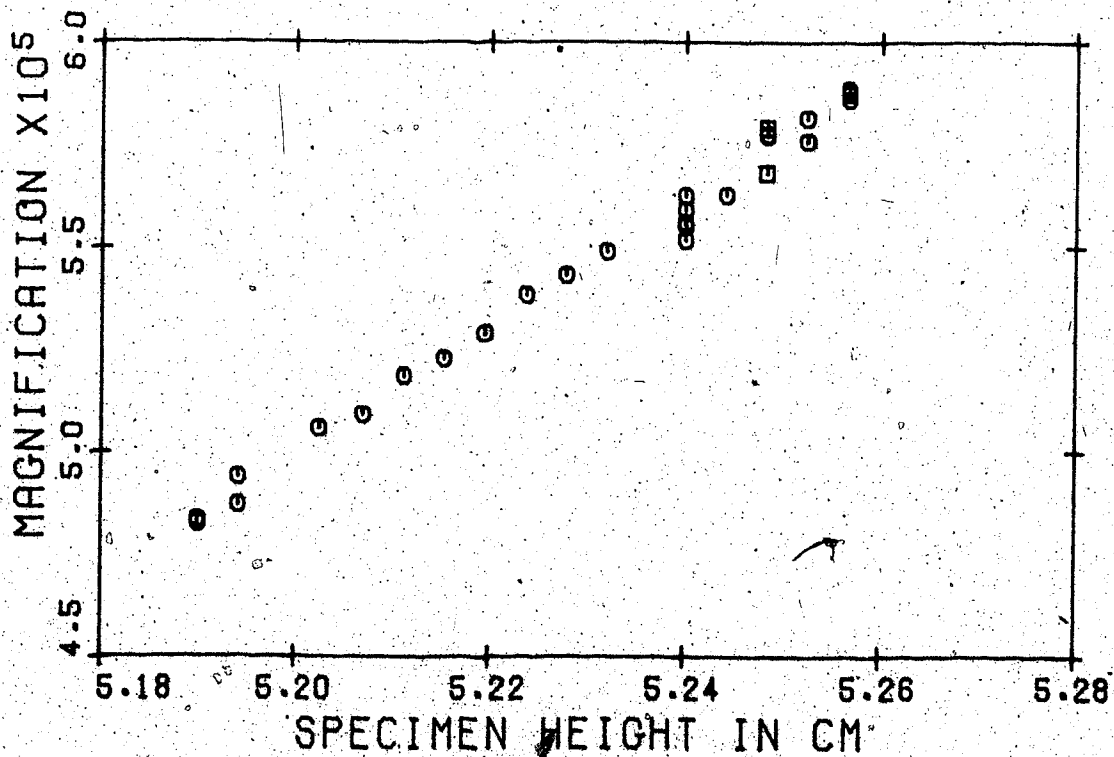


Figure (17) Magnification as a function of specimen height.



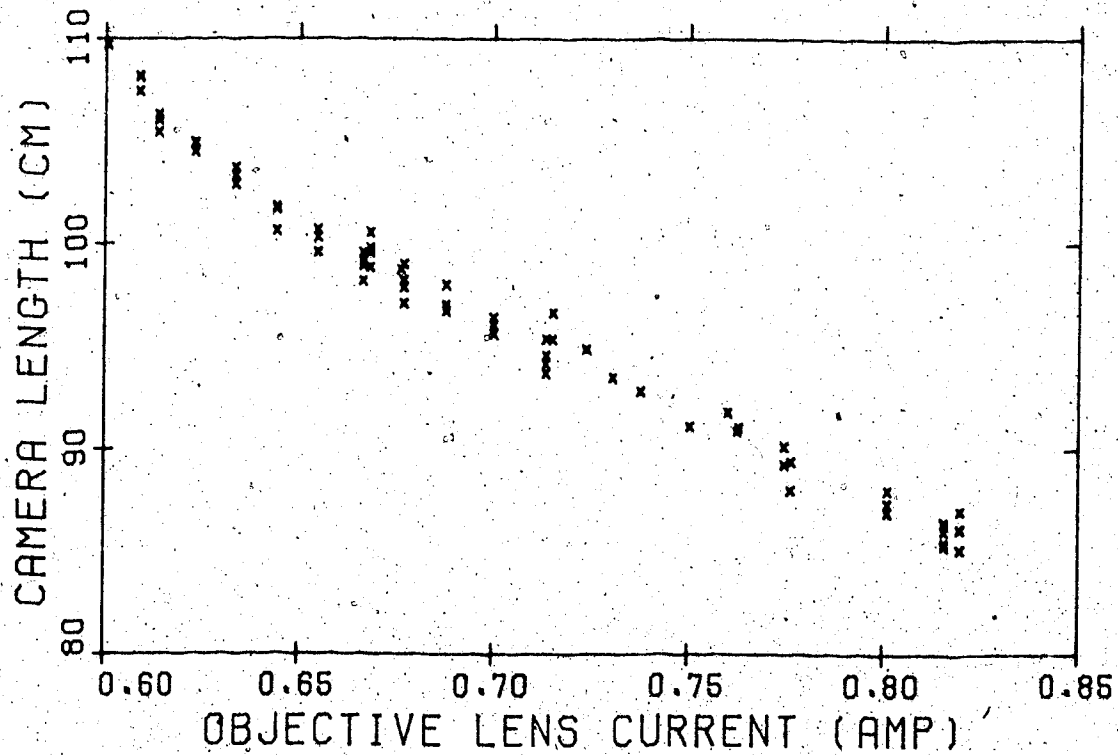


Figure (18) The camera length (nominally 80 cm) as a function of the objective lens current.

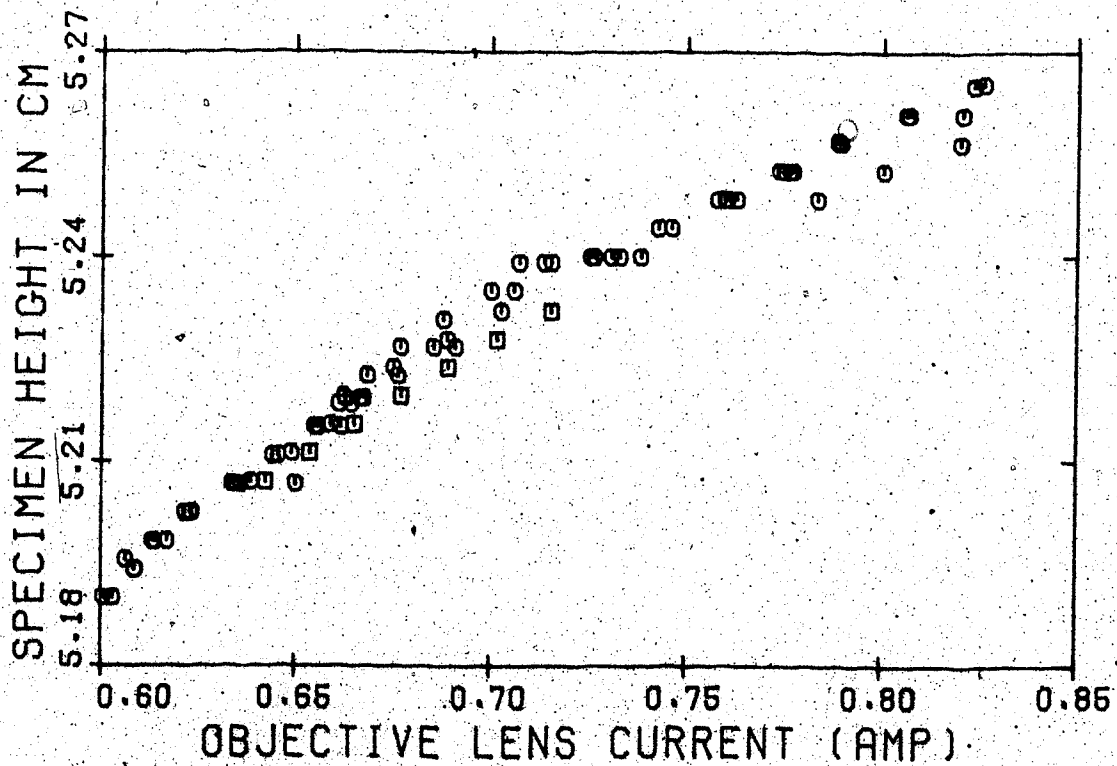


Figure (19) Specimen height plotted against objective lens current for an infocus specimen.

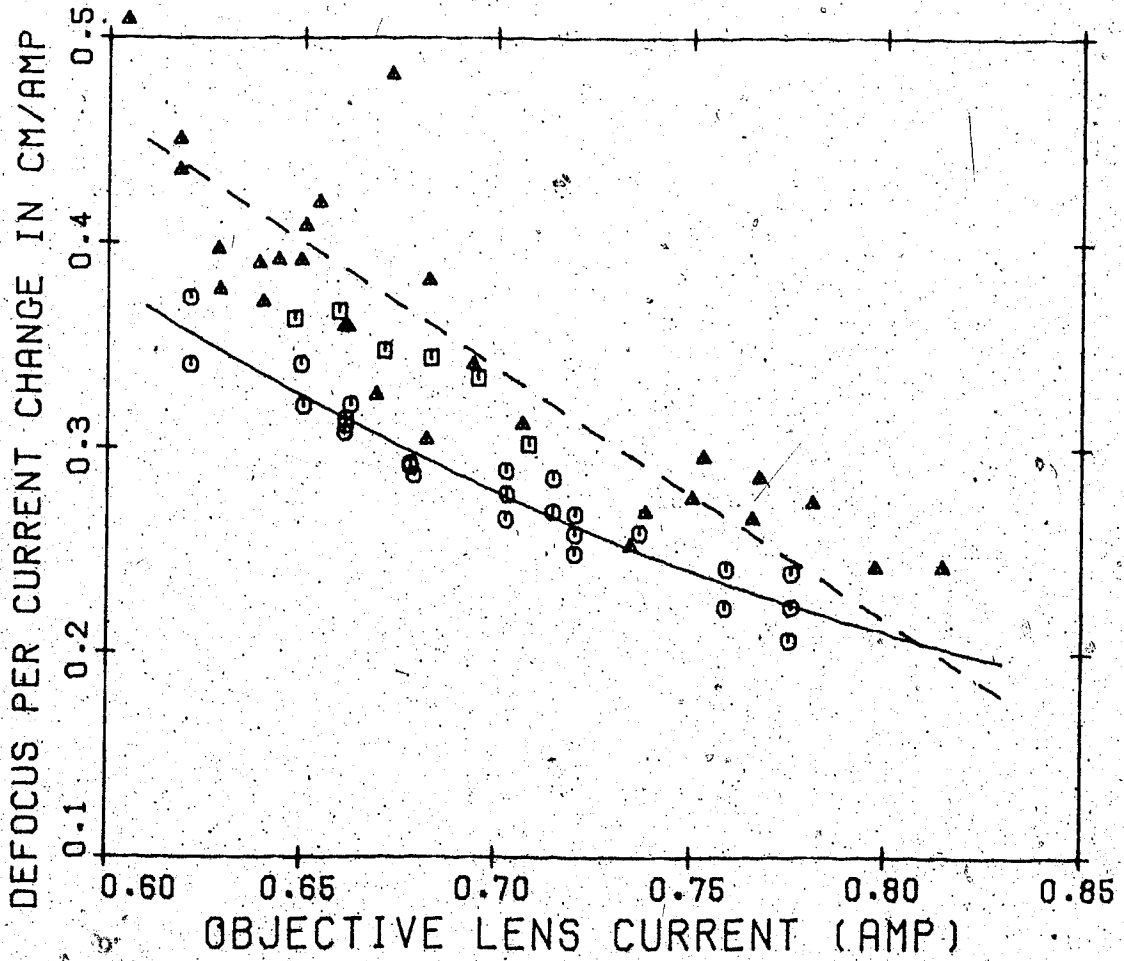


Figure (20) The amount of defocus per current change obtained by various methods.



a.



b.

Figure (21) Examples of defocus dependence determinations using doubly exposed micrographs of diffracted MgO beams in untilted dark field mode.  
a. Using a (220) beam.  
b. Using a (200) beam.

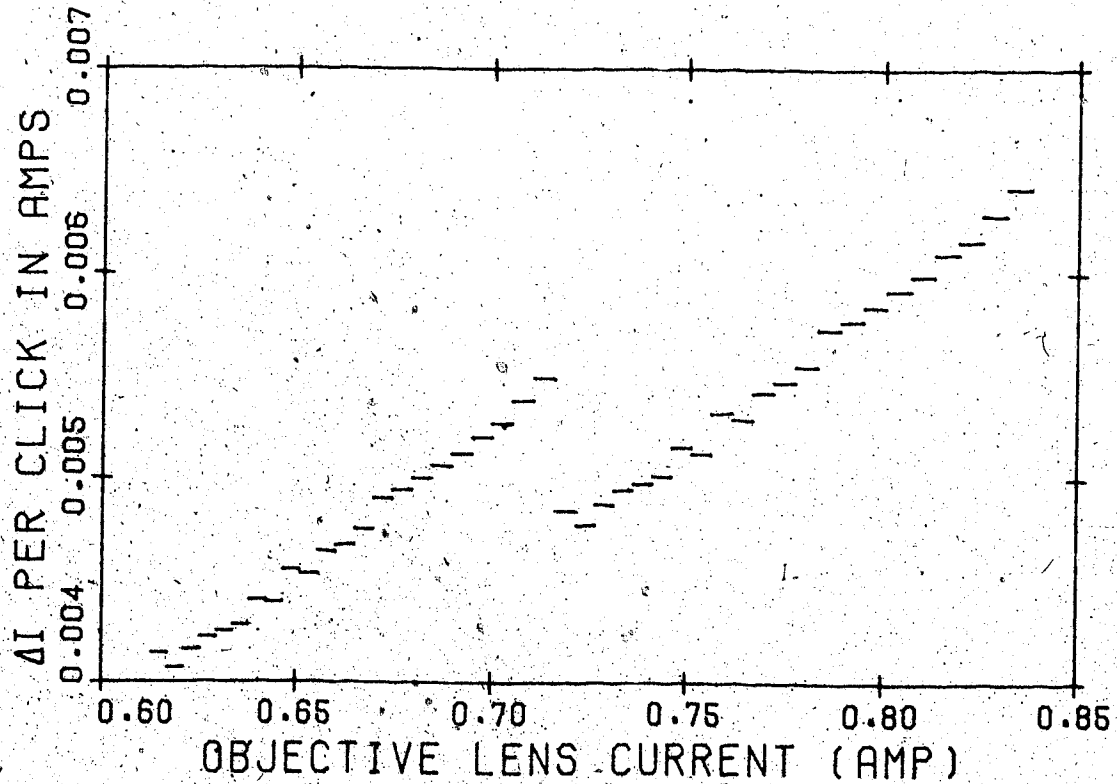


Figure (22) The change in objective lens current per click of the medium knob. The discontinuity occurs where the coarse knob is changed.

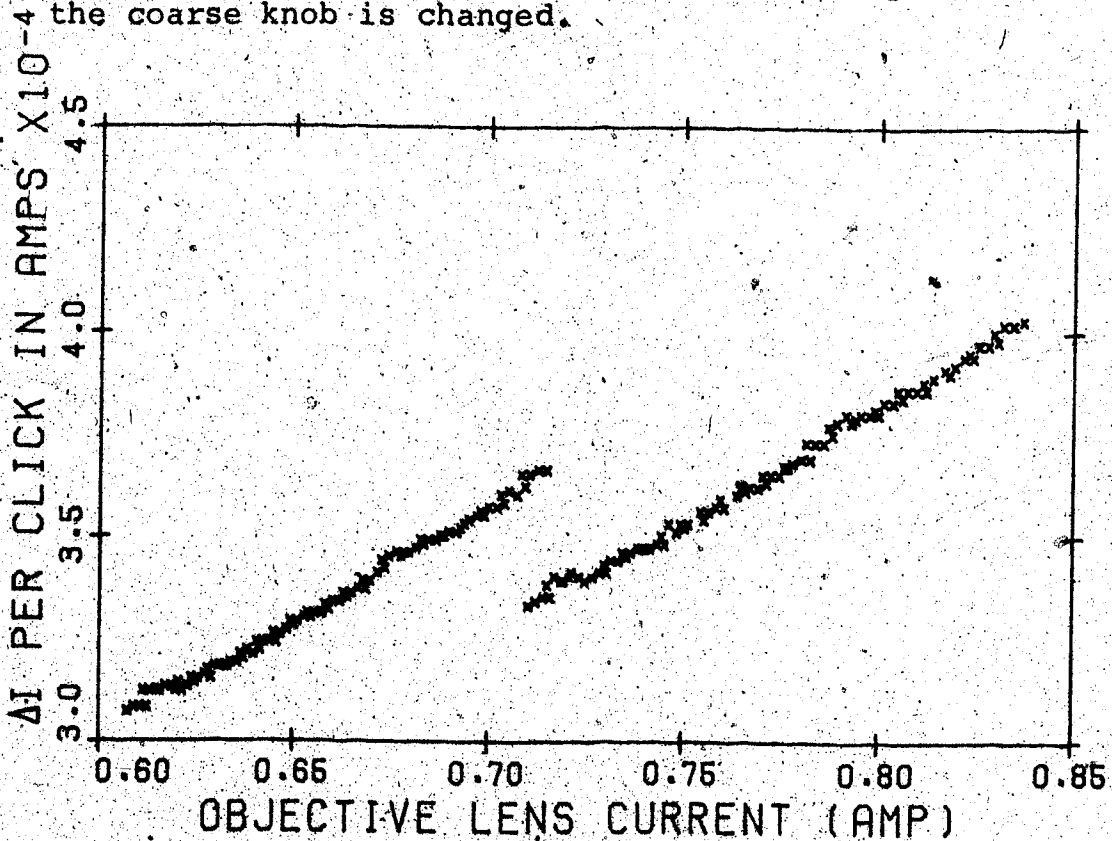


Figure (23) The change in objective lens current per click of the fine medium knob. Each data point is the average of five clicks.

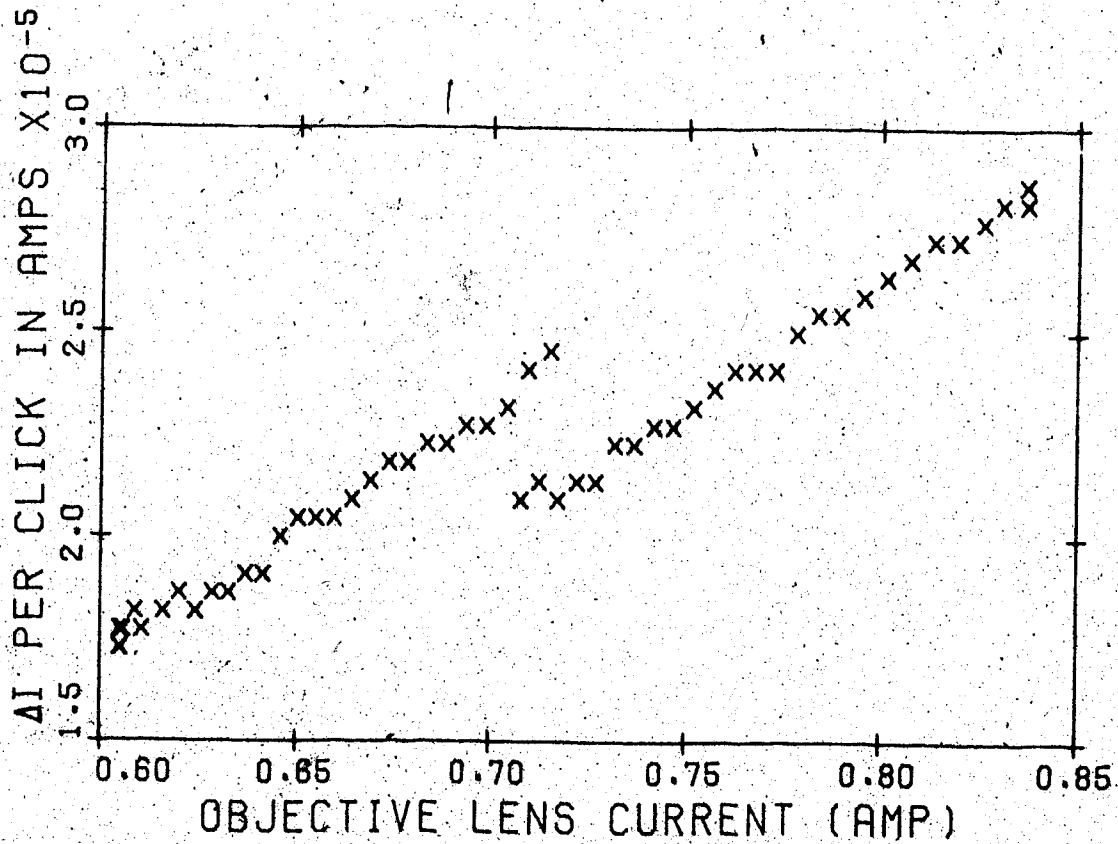


Figure (24) The change in objective lens current per click of the second finest knob. Each data point is the average of 22 clicks. The discontinuity occurs where the coarse knob is changed.

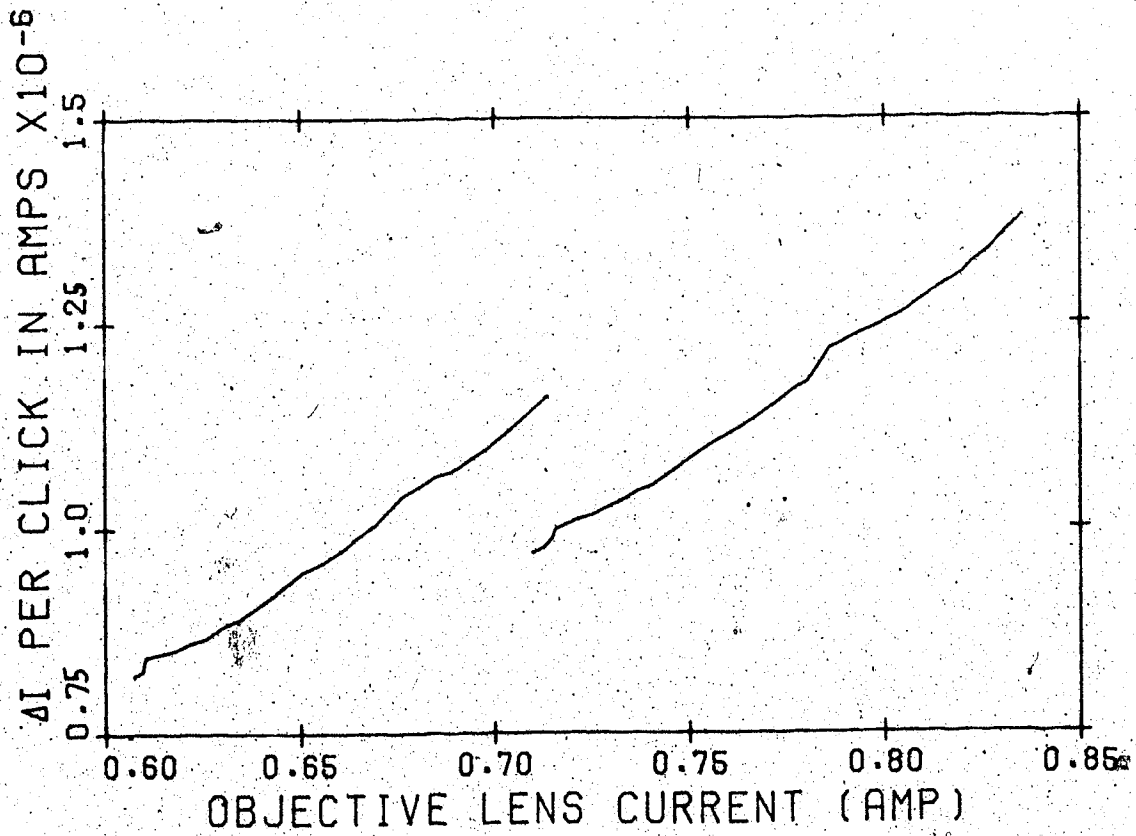


Figure (25) The change in objective lens current per click of the finest knob. The graph is  $1/16.32$  of the data for the second finest knob.

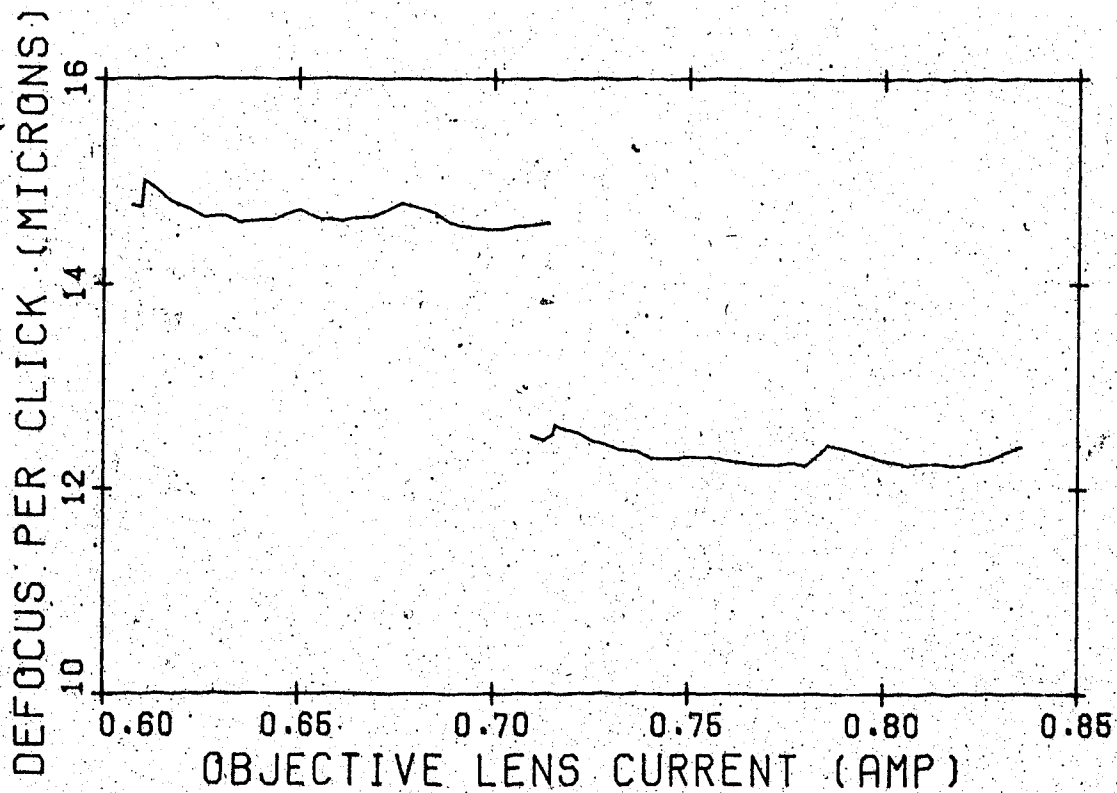


Figure (26) The amount of defocus per click of the medium knob. The discontinuity occurs when the coarse knob is changed.

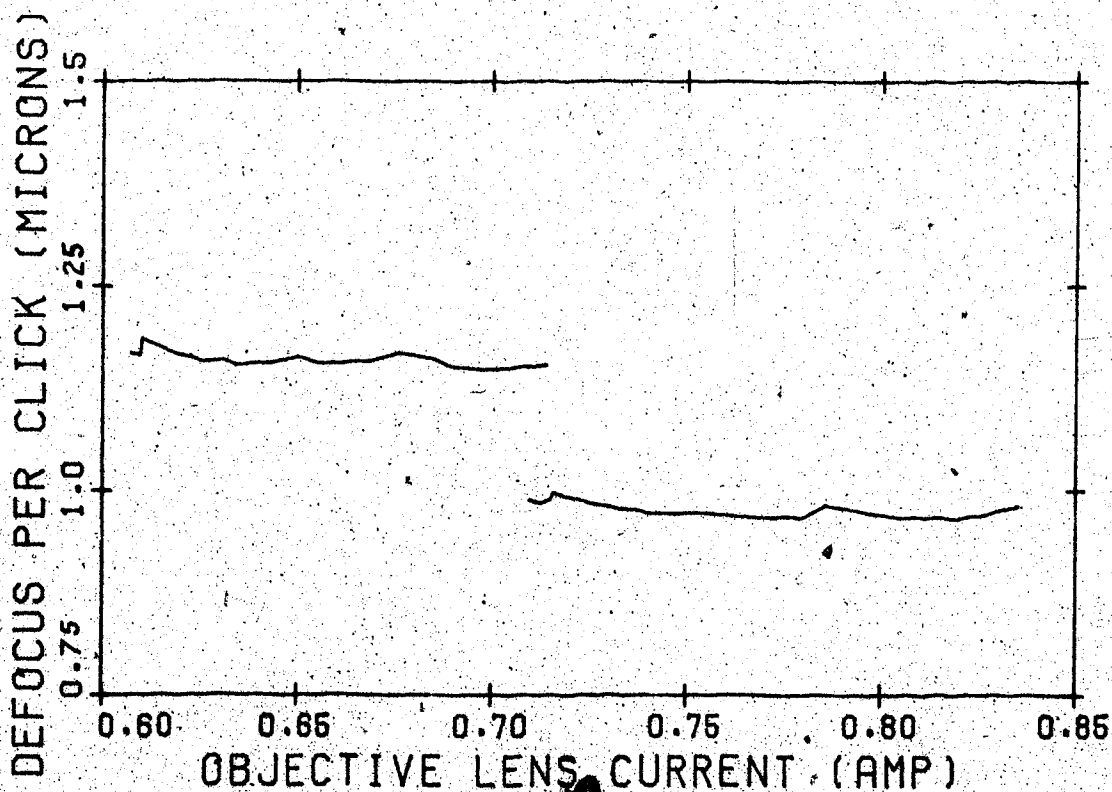


Figure (27) The amount of defocus per click of the fine medium knob.

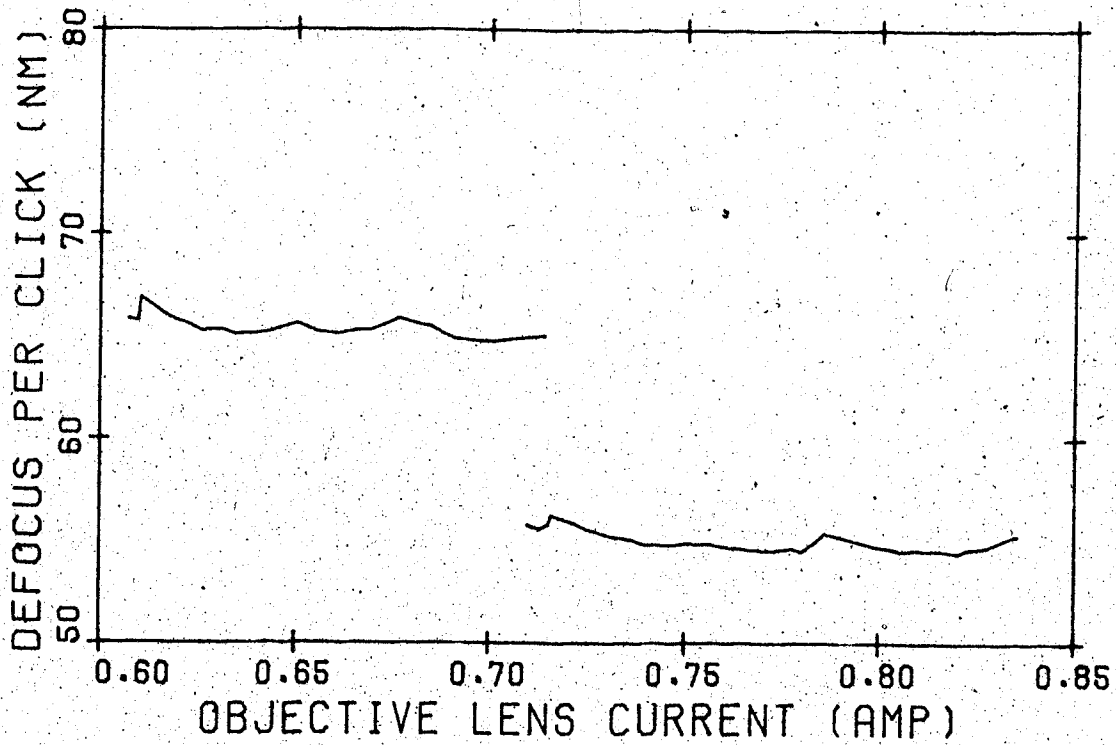


Figure (28) The amount of defocus per click of the second finest knob. The discontinuity occurs when the coarse knob is changed.

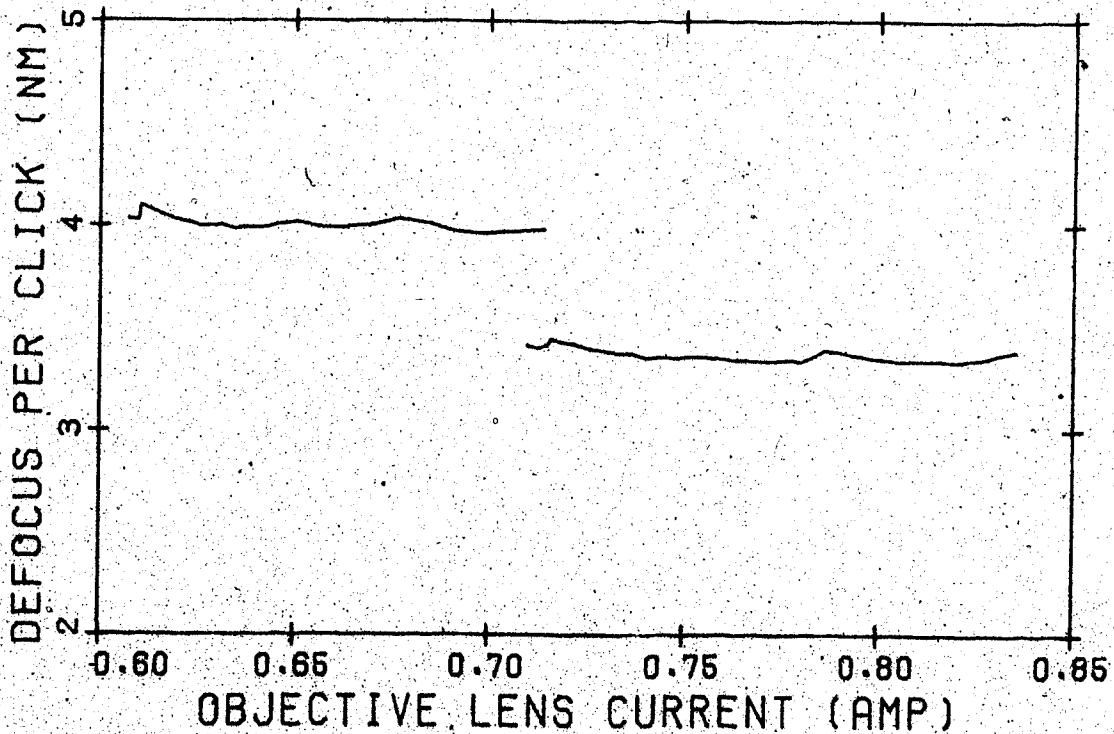


Figure (29) The amount of defocus per click of the finest knob.



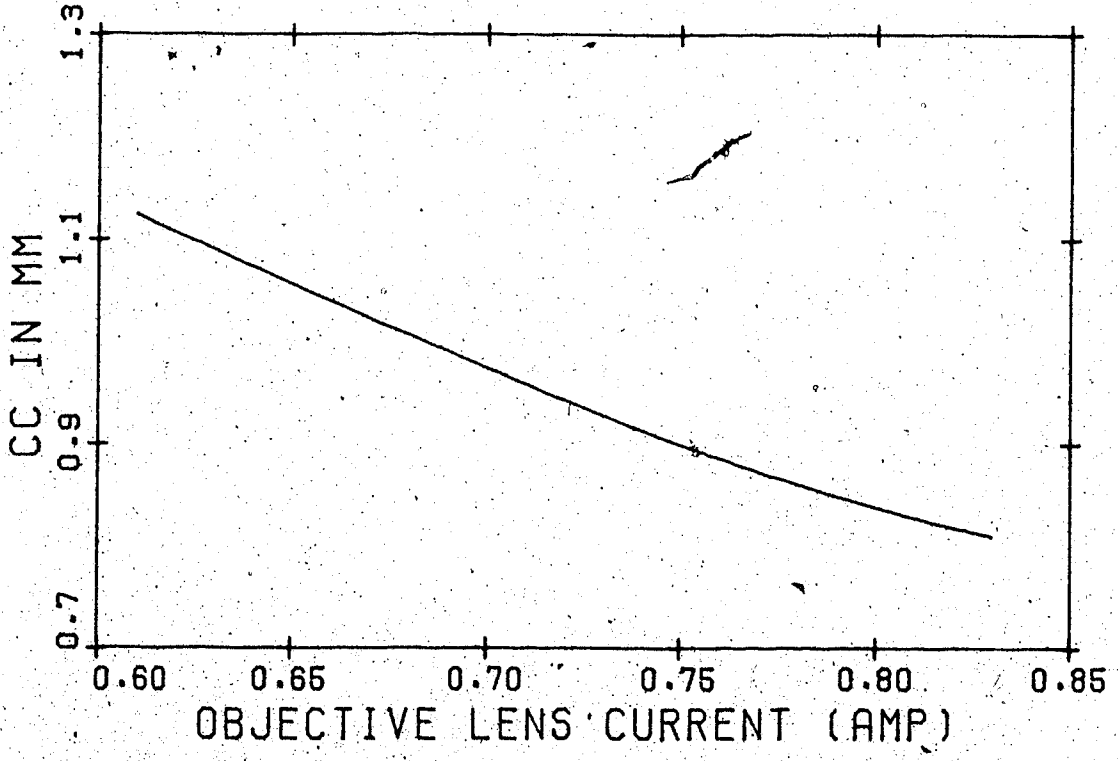


Figure (30) The upper limit of the chromatic aberration coefficient as a function of the objective lens current.

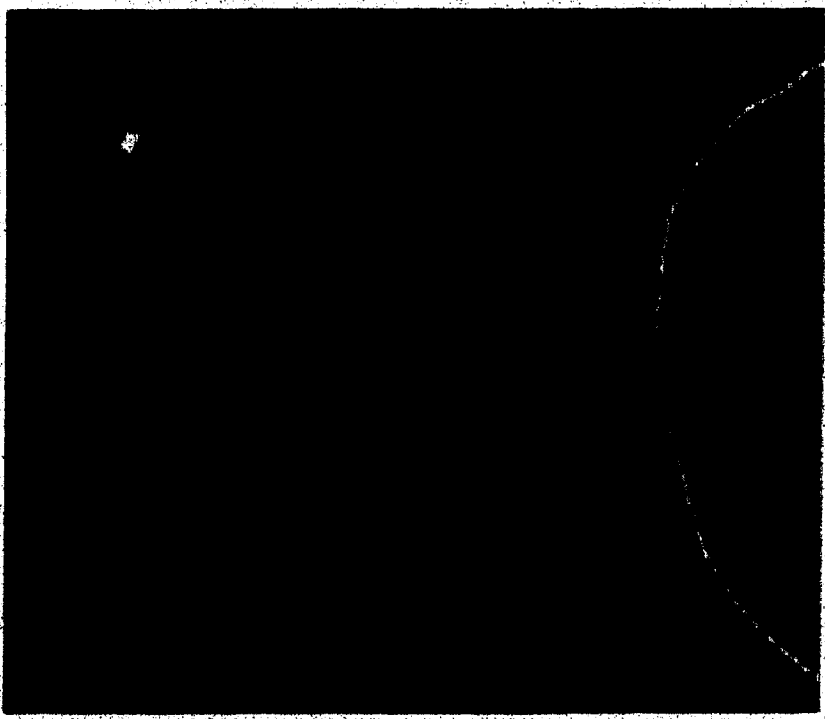


Figure (31) A photograph of amorphous carbon and the corresponding diffractogram.

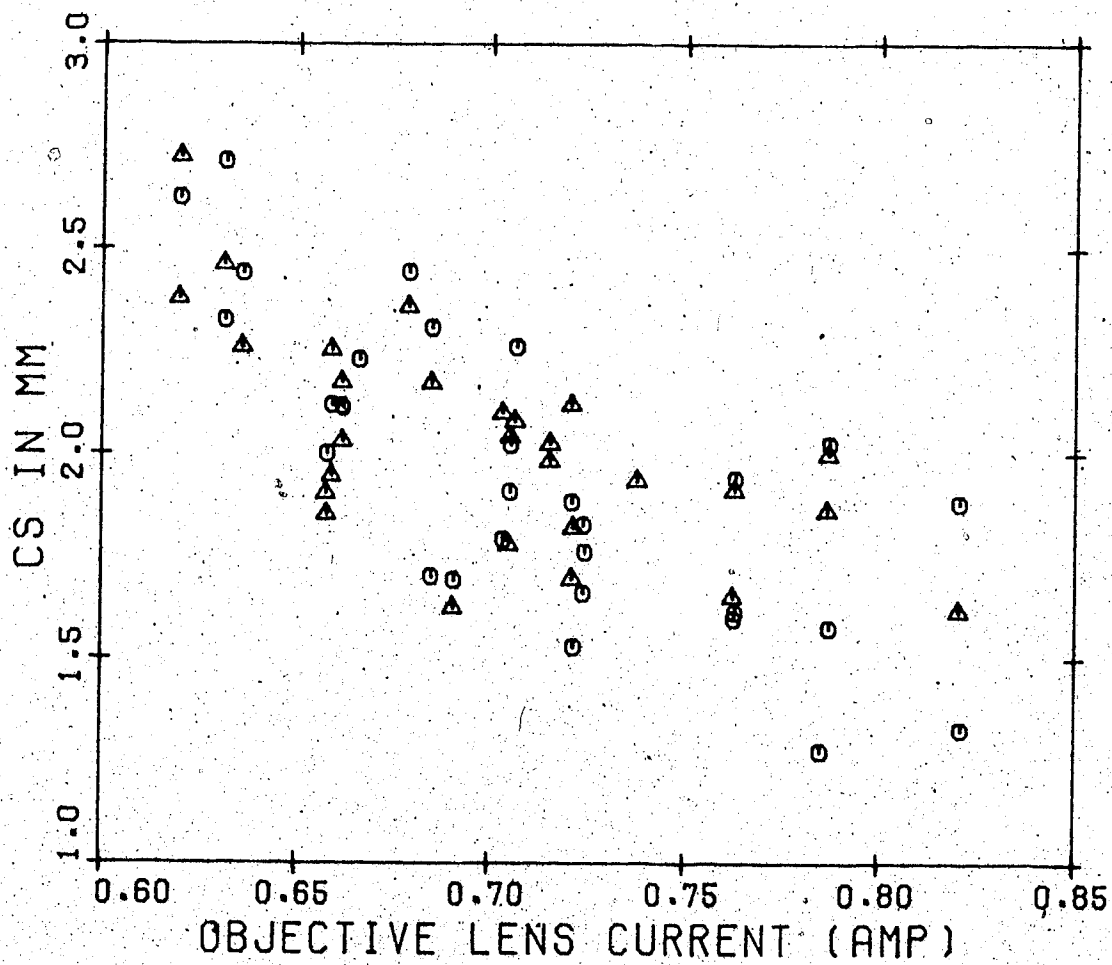


Figure (32) The spherical aberration coefficient measured by two methods. The data in triangles were obtained by the method due to Heinemann (1971). The circles were obtained by the Hall (1949) method.

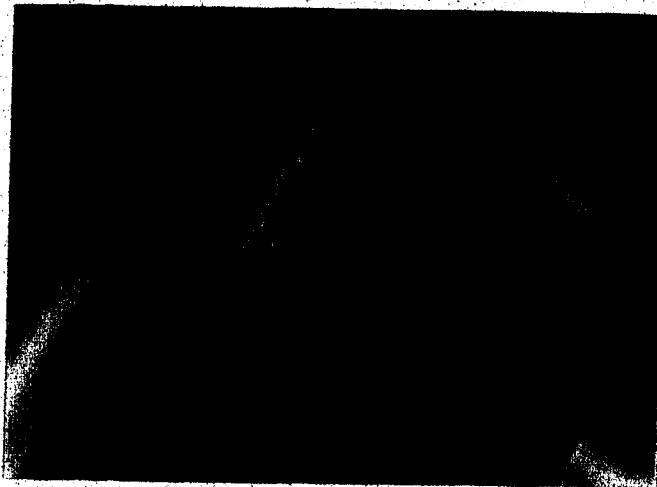
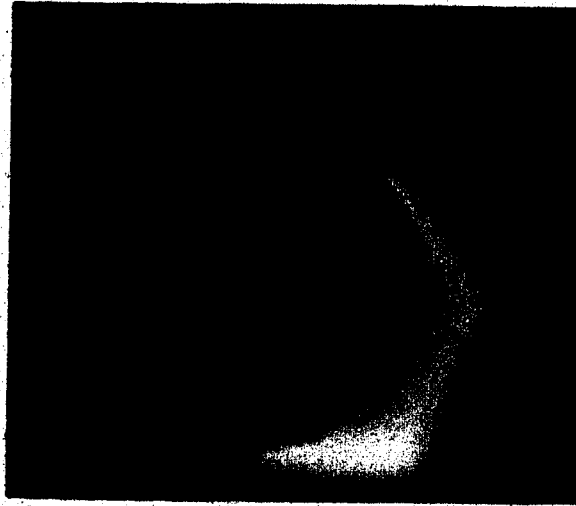


Figure (33) Examples of measurements to determine the spherical aberration coefficient. The central beam image is in focus in the direction in which the diffracted beam image is displaced. Both examples use a (220) beam of MgO.

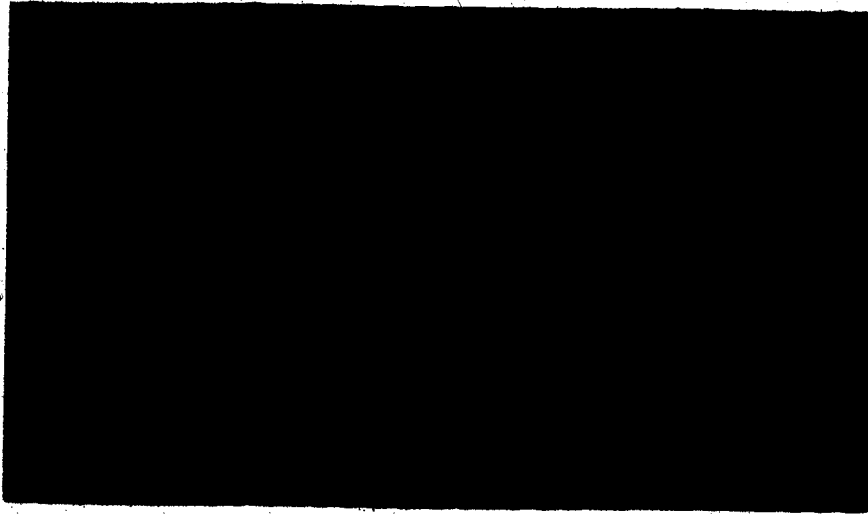
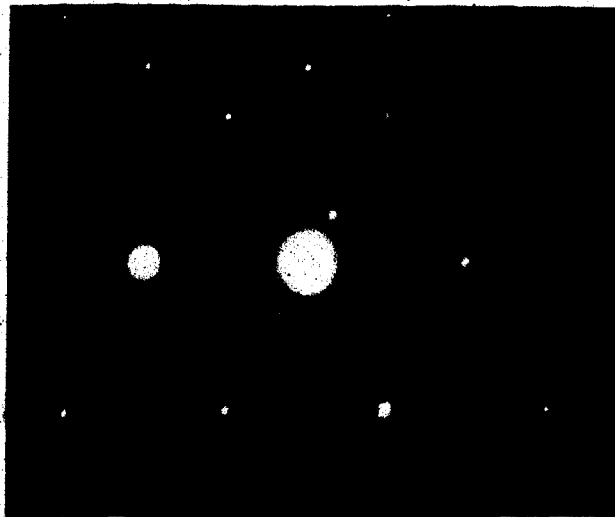


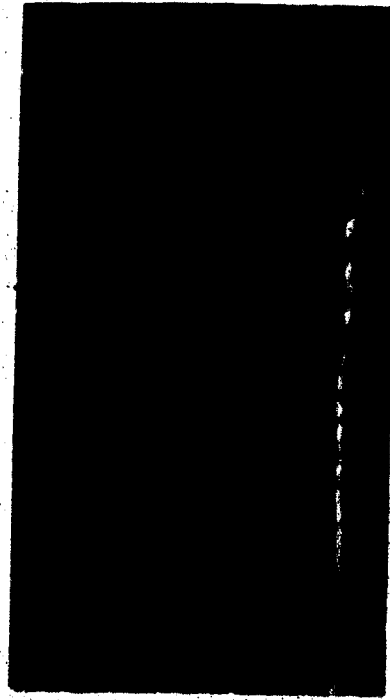
Figure (34) a. Crossed lattice fringes of biotite: strongly in two directions and weakly in a third.



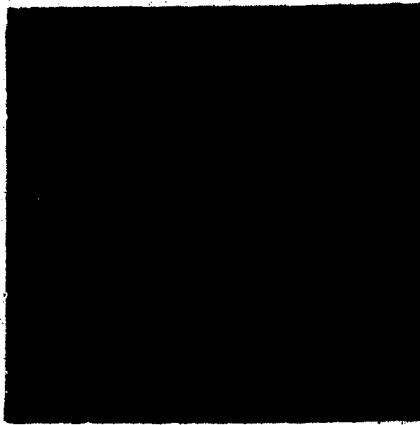
b. The (hk0) diffraction pattern of biotite. The 3-fold crossed lattice fringes were obtained in the untilted bright field mode, with the objective aperture transmitting only the central beam and the six lowest order diffracted beams.



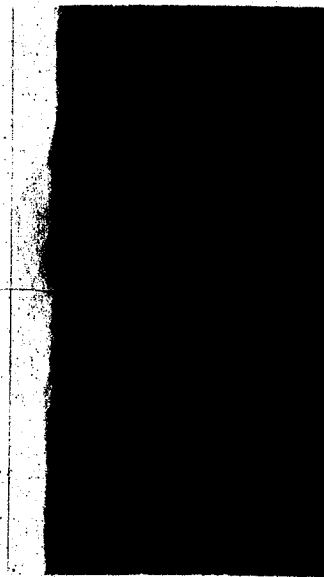
a



b



c



d

Figure (35) Edge on views of biotite (a. and b.), and muscovite (c. and d.).

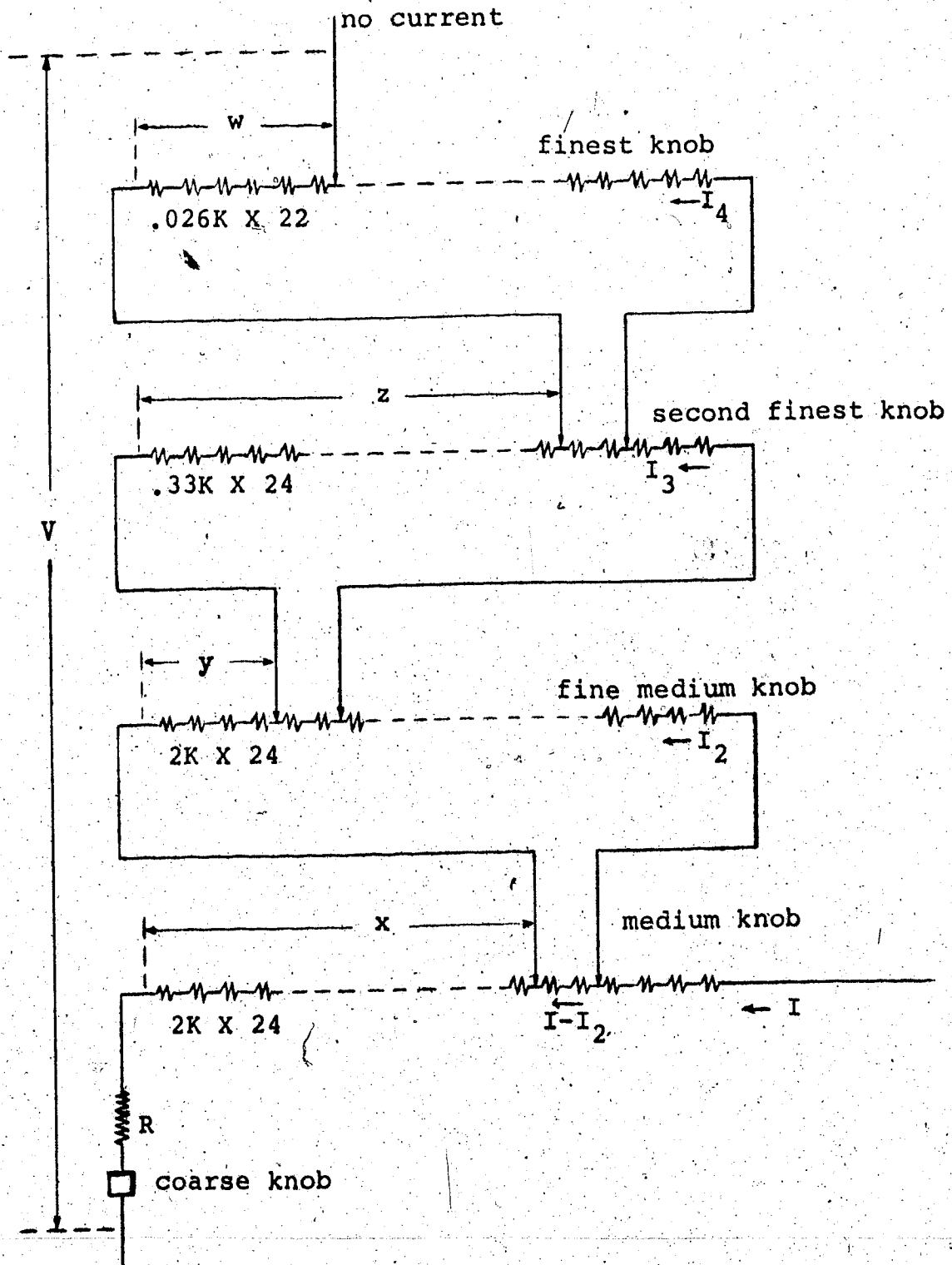


Figure (36) A schematic diagram of the objective lens current control circuit.

## REFERENCES

- Allpress, J.G. and Sanders, J.V. (1973), J. Appl. Cryst. 6, 165.
- Beeston, B.E.P., Horne, R.W. and Markham, R. (1972), Electron Diffraction and Optical Diffraction Techniques, North-Holland.
- Born, M. and Wolf, E. (1970), Principles of Optics, 4 ed., Pergamon, Oxford.
- Bragg, W.L. (1937), Atomic Structure of Minerals, Cornell University Press.
- Buseck, P.R. and Iijima, S. (1974), Am. Mineral. 59, 1.
- Cockayne, D.J.H., Parsons, J.R., Hoelke, C.W. (1971), Phil. Mag. 24, 139.
- Cowley, J.M. (1959), Acta Cryst. 12, 367.
- Cowley, J.M. (1973), Acta Cryst. A29, 529.
- Cowley, J.M. and Iijima, S. (1972), Z. Naturforsch. 27a, 445.
- Cowley, J.M. and Kuwabara, S. (1962), Acta Cryst. 15, 260.
- Cowley, J.M. and Moodie, A.F. (1957), Acta Cryst. 10, 609.
- Cowley, J.M. and Moodie, A.F. (1958), Proc. Phys. Soc. 71, 533.
- Cowley, J.M. and Moodie, A.F. (1959a), Acta Cryst. 12, 353.
- Cowley, J.M. and Moodie, A.F. (1959b), Acta Cryst. 12, 360.
- Chemical Rubber Co., Handbook of Chemistry and Physics, 53 ed., 1972.
- Crystal Data Determinative Tables, Vol. 2, 3 ed. (1973), edited by J.D.H. Donnay and H.M. Ondik, Published jointly by the U.S. Department of Commerce, National Bureau of Standards, and the Joint Committee on Powder Diffraction Standards.
- Eisenhandler, C.B. and Siegel, B.M. (1966), J. Appl. Phys. 37, 1613.
- El Kareh, A.B. and El Kareh, J.C.J. (1970), Electron Beams, Lenses, and Optics, Vol. 2, Academic Press.

- Formanek, H., Müller, M., Hahn, M.H., Koller, T. (1971), Naturwissenschaften 58, 339.
- Haine, M.E. and Cosslett, V.E. (1961), The Electron Microscope: The Present State of the Art, E.&F.N. Spon Ltd., London.
- Hall, C.E. (1949), J. Appl. Phys. 20, 631.
- Hall, C.R. and Hines, R.L. (1970), Phil. Mag. 21, 1175.
- Hanszen, K-J. (1971), 'Optical Transfer Theory of the Electron Microscope', in Advances in Optical and Electron Microscopy, Vol. 4, edited by R. Barer and V.E. Cosslett, Academic Press.
- Hashimoto, H., Kumao, A., Hino, K., Endoh, H., Yotsumoto, H., Ono, A. (1973). J. Elec. Mic. 22, 123.
- Hashimoto, H., Kumao, A., Hino, K., Yotsumoto, H., Ono, A. (1971), Japan J. Appl. Phys. 10, 1115.
- Hashimoto, H., Mannami, M., Naiki, T. (1961), Phil. Trans. A253, 459.
- Hashimoto, H. and Watanabe, H. (1960), Nature 188, 571.
- Hawkes, P.W. (1972), Electron Optics and Electron Microscopy, Taylor and Francis Ltd., London.
- Heidenreich, R.D. (1964), Fundamentals of Transmission Electron Microscopy, Interscience Publishers.
- Heinemann, K. (1971), Optik 34, 113.
- Henkelman, R.M. and Ottensmeyer, F.P. (1971), Proc. Nat. Acad. Sci. USA 68, 3000.
- Hoppe, W. (1961), Naturwiss. 48, 736.
- Krakow, W., Downing, K.H., Siegel, B.M. (1974), Optik 40, 1.
- Lenz, F.A. (1970), in Electron Microscopy in Material Science, 1970 International School of Electron Microscopy, edited by U. Valdrè, Academic Press (1971).
- McGillivray, D.J. (1975), M.Sc. Thesis to be published, University of Alberta, Department of Physics.



- Menter, J.W. (1956), Proc. Roy. Soc. A236, 119.
- Ottensmeyer, F.P., Schmidt, E.E., Olbrecht, A.J. (1973),  
Science 179, 175.
- Parsons, J.R., Johnson, H.M., Hoelke, C.W., Hosbons, R.R.  
(1973), Phil. Mag. 27, 1359.
- Phillips, V.A., Chalk, A.J., Hugo, J.A. (1972), J. Elec.  
Mic. 21, 323.
- Prestridge, E.B. and Yates, D.J.C. (1971), Nature 234,  
345.
- Rebsch, R. (1938), Ann. d. Phys. 31, 551.
- Reimer, L. (1969), Z. Naturforsch. A24, 377.
- Scherzer, O. (1936), Z. Phys. 101, 593.
- Scherzer, O. (1949), J. Appl. Phys. 20, 20.
- Squires, G.L. (1968), Practical Physics, McGraw-Hill,  
London.
- Thon, F. (1970), in Electron Microscopy in Material  
Science, 1970 International School of Electron  
Microscopy, p. 571, edited by U. Valdrè, Academic  
Press (1971).
- Thon, F. and Willasch, D. (1972), Optik 36, 55.
- Turner, P.S. (1965), M. Sc. Report (Unpublished),  
University of Melbourne, School of Physics.
- Vorobev, Y.V. and Vyazigin, A.A. (1967), Optics Spectr.  
22, 261.

## APPENDIX I

### THE LIGHT OPTICAL DIFFRACTOMETER

The spatial frequency spectrum present in a micrograph can be obtained with a light optical diffractometer. The micrograph is illuminated with parallel, monochromatic, coherent light. The transmitted light is focussed on a screen or on a photographic plate to obtain the Fraunhofer diffraction pattern. Maxima occur in the diffraction plane at scattering angle  $\theta$  according to the grating equation:

$$d \sin \theta = n \lambda_2$$

where  $\lambda_2$  is the wavelength of the monochromatic light, and  $d$  is some spacing present in the photograph. The radial distance  $q$  from the optic axis at the diffraction plane is related to  $\theta$  by

$$\tan \theta = q/L$$

where  $L$  is the camera length of the diffractometer.

Since  $\theta$  is small ( $q \ll L$ ), the approximation

$\sin \theta \approx \tan \theta$  is valid. Therefore

$$d q/L = n \lambda_2$$

or  $d q = n \lambda_2 L$

Instead of letting  $n$  indicate the diffraction order,  $d$  shall be allowed to do so, and  $n$  shall be fixed at 1. If the photograph used is an electron micrograph, then the spacings  $d$  which are present are related to the electron scattering angles by

$$d = M \lambda_1 / \alpha$$

Thus

$$M \lambda_1 q / \alpha = \lambda_2 L$$

or

$$\alpha = M \lambda_1 q / \lambda_2 L$$

Here  $\lambda_1$  is the electron wavelength (0.0037 nm at 100 KeV). Thus  $\alpha$  or  $d$  can be calculated from  $q$  once the various constants are known.

In practice the diffractometer can be simplified somewhat by illuminating the specimen with slightly convergent light. The equations still hold to very good accuracy. The actual diffractometer that was used is described by McGillivray (1975). An excellent explanation of optical diffractometry is found in Beeston, Horne, and Markham (1972).

## APPENDIX II

### ANALYSIS OF OBJECTIVE LENS CURRENT CONTROL CIRCUIT

The objective lens current is controlled by 5 knobs: a coarse knob, a medium knob, a fine medium knob, a second finest knob, and a fine knob. We consider only the effect of the 4 finer ones here. These are sliding controls which tap banks of resistors, shown schematically in Figure (36). The medium knobs and the second finest knob straddle two resistors. The finest knob has only one contact which does not draw any current.

The current is regulated by comparing the voltage  $V$  to a reference voltage  $V_0$ . To calculate the effect of the various knobs, it is necessary to do a circuit analysis:

$$V_4 = I_4 \cdot 22(.062K) = 1.364K I_4 \quad (K = \text{kilohms})$$

$$V_3 = I_3 [22(.33K) + .66K(1.364K) / (.66K + 1.364K)] = 7.7K I_3$$

$$V_2 = I_2 [22(2K) + 4K(7.7K) / (4K + 7.7K)] = 46.6K I_2$$

$$\text{But } V_2 = (I - I_2)4K \quad \text{or} \quad 46.6K I_2 = 4K I - 4K I_2$$

$$\text{Therefore } I_2 = .079 I.$$

$$V_3 = (I_2 - I_3)4K \quad \text{or} \quad 7.7K I_3 = 4K I_2 - 4K I_3$$

$$\text{Therefore } I_3 = .34 I_2 = .027 I.$$

$$V_4 = (I_3 - I_4) \cdot 66K \quad \text{or} \quad 1.364K I_4 = .66K I_3 - .66K I_4.$$

$$\text{Therefore } I_4 = .326 I_3 = .0088 I.$$

Let the four knobs be x, y, z, and w clicks from the zero position, as in the figure. R is a large resistance (> 240K). Then

$$V = IR + x \cdot 2K I + y \cdot 2K \cdot .079I + z \cdot .33K \cdot .027I + w \cdot .062K \cdot .0088I.$$

Now, because of the feedback,

$$I = k(V - V_0) \quad \text{or} \quad V = V_0 + I/k, \quad k \text{ a constant.}$$

$$\text{Therefore } I = V_0 [R + 2Kx + .158Ky + .0089Kz + .000546Kw - 1/k]^{-1}.$$

The change in current upon changing the medium knob by one click is

$$\begin{aligned} \Delta I_m &= V_0 [R + 2K(x+1) + .158Ky + .0089Kz + .000546Kw - 1/k]^{-1} \\ &\quad - V_0 [R + 2Kx + .158Ky + .0089Kz + .000546Kw - 1/k]^{-1} \\ &= V_0 (-2K) [R + 2Kx + 2K + .158Ky + .0089Kz + .000546Kw - 1/k]^{-1} \\ &\quad \cdot [R + 2Kx + .158Ky + .0089Kz + .000546Kw - 1/k]^{-1}. \end{aligned}$$

Similarly,

$$\begin{aligned} \Delta I_{fm} &= V_0 (-0.158K) [R + 2Kx + .158(y+1) + .0089Kz + .000546Kw - 1/k]^{-1} \\ &\quad \cdot [R + 2Kx + .158Ky + .0089Kz + .000546Kw - 1/k]^{-1} \end{aligned}$$

$$\Delta I_{sf} = V_o (-.0089K) [R+2Kx+.158Ky+.0089K(z+1)+.00546Kw-1/k]^{-1} \\ \cdot [R + 2Kx + .158Ky + .0089Kz + .000546Kw - 1/k]^{-1}$$

$$\Delta I_f = V_o (-.000546K) [R+2Kx+.158Ky+.0089Kz+.000546K(w+1)-1/k]^{-1} \\ \cdot [R + 2Kx + .158Ky + .0089Kz + .000546Kw - 1/k]^{-1} .$$

Thus the ratios between the various knobs are, to a very good approximation:

$$\frac{\Delta I_m}{\Delta I_{fm}} = \frac{2}{.158} = 12.66$$

$$\frac{\Delta I_{fm}}{\Delta I_{sf}} = \frac{.158}{.0089} = 17.73$$

$$\frac{\Delta I_{sf}}{\Delta I_f} = \frac{.0089}{.000546} = 16.32 .$$

These are the ratios of the focussing strengths of the various knobs.